Nutrient metabolism regulates insulin granule formation in the pancreatic islet β-cell via ER redox homeostasis

Kristen E. Rohli[1,2,3], Cierra K. Boyer[1,4], Shelby C. Bearrows[1,3], Marshall R. Moyer[1,3], Weston S. Elison[5], Casey J. Bauchle[1,3], Sandra E. Blom[1,3], Chi-Li Yu[6], Marshall R. Pope[6], Jianchao Zhang[7], Yanzhuang Wang[7,8], and Samuel B. Stephens[1,2,3,9]

[1]Fraternal Order of Eagles Diabetes Research Center, University of Iowa, Iowa City, IA, USA
[2]Interdisciplinary Graduate Program in Genetics, University of Iowa, Iowa City, IA, USA
[3]Department of Internal Medicine, Division of Endocrinology and Metabolism, University of Iowa, Iowa City, IA, USA
[4]Department of Pharmacology, University of Iowa, Iowa City, IA, USA
[5]Department of Nutrition, Dietetics, and Food Science, Brigham Young University, Provo, Utah, USA
[6]Proteomics Facility, University of Iowa, Iowa City, IA, USA
[7]Department of Molecular, Cellular, and Developmental Biology, University of Michigan, Ann Arbor, MI, USA
[8]Department of Neurology, School of Medicine, University of Michigan, Ann Arbor, MI, USA

[9]Corresponding author:
Samuel B. Stephens, Ph.D.
Fraternal Order of Eagles Diabetes Research Center
Department of Internal Medicine, Division of Endocrinology and Metabolism
University of Iowa
Iowa City, IA 52246
Email: samuel-b-stephens@uiowa.edu
Tel. 319-335-4843

Running title: Mitochondrial dysfunction impairs proinsulin trafficking

Key words: endoplasmic reticulum, protein folding, redox, glutathione, proinsulin trafficking, secretory granule formation, β-cell function, mitochondria, insulin, NAPDH

Abstract

Defects in the pancreatic β-cell's secretion system are well-described in Type 2 diabetes (T2D) and include impaired proinsulin processing and a deficit in mature insulin-containing secretory granules; however, the cellular mechanisms underlying these defects and the contribution of hyperglycemia to this process remain poorly understood. Here, we used an *in situ* fluorescent pulse-chase strategy and proximity labeling-based quantitative proteomics analysis to study proinsulin trafficking and demonstrate a direct link to glucose metabolism via the production of redox intermediates that facilitate proinsulin export from the ER. We show that ER export of proinsulin is delayed in T2D models resulting in decreased insulin granule formation and further demonstrate this process can be regulated by NADPH and reducing equivalent availability. Together, these data highlight a critical role for nutrient metabolism and mitochondrial dysfunction in the maladaptive remodeling of the β-cell's secretory pathway in the decline of β-cell function in T2D.

46 **Introduction**

47 In the pancreatic islet β-cell, metabolic fuel sensing functions at multiple levels to coordinate
48 insulin secretory capacity with physiological demands of nutrient status (Boland et al., 2017).
49 For example, ATP and other metabolic signals generated by glucose oxidation directly trigger
50 and amplify insulin granule exocytosis through membrane depolarization and insulin granule
51 recruitment (Gembal et al., 1992; Henquin, 2009; Henquin et al., 2002). In addition,
52 mitochondrial metabolism of glucose and other fuels stimulates the translation of preproinsulin
53 mRNA through a stem-loop structure in the 5'UTR, as well as ~50 other mRNAs associated with
54 insulin granules (Guest et al., 1989; Uchizono et al., 2007; Wicksteed et al., 2003), to ensure that
55 β-cells meet or exceed the physiological demands of insulin release with insulin biosynthesis.
56 Nutrient challenge can also elicit more global changes in β-cell secretory function, such as
57 during prolonged fasting, which results in a pronounced reduction in the β-cell's insulin
58 secretory capacity, including insulin degranulation and increased numbers of autophagosomes
59 and lysosomes, as part of a physiological mechanism to limit insulin release and thereby ward off
60 hypoglycemia (Boland et al., 2018). Collectively, these observations illustrate the β-cell's ability
61 to use metabolic fuels as hierarchal signals to modulate secretory functions.

62

63 Loss of β-cell secretory function and insulin insufficiency have been identified as critical events
64 in the progression of insulin resistance to Type 2 diabetes (T2D), yet the underlying cellular
65 mechanisms are not well understood (Halban et al., 2014; Kahn et al., 2009). Overt changes in
66 the β-cell's secretory pathway accompany the onset of T2D and include decreased numbers of
67 insulin-containing secretory granules, proinsulin processing deficiencies, and

68 hyperproinsulinemia (Alarcon et al., 2016; Kahn and Halban, 1997; Like and Chick, 1970;
69 Masini et al., 2012; Ward et al., 1984). While increased insulin exocytosis and proinsulin/insulin
70 degradation likely contribute to the overall deficit in available insulin supply in T2D (Pasquier et
71 al., 2019; Rhodes and Alarcon, 1994; Shrestha et al., 2020, p. 1), perturbations in the
72 ultrastructure of the β-cell secretory organelles (ER, Golgi, autophagosomes) suggest that
73 alterations in early stages of proinsulin sorting and trafficking also contribute to the insulin
74 insufficiency in T2D (Alarcon et al., 2016; Like and Chick, 1970; Masini et al., 2012). Studies
75 on early stages of proinsulin trafficking and insulin granule formation have been challenging, in
76 part, due to the prolonged half-life of proteins within the mature secretory granule, such as
77 insulin (t ½ ~ 2.7 days) (Muller et al., 2017), which are also highly abundant. Nevertheless,
78 defects in proinsulin trafficking and insulin granule formation can directly decrease insulin
79 secretory capacity (Bearrows et al., 2019; Cao et al., 2013, p. 1; Stephens et al., 2017) and may
80 occur in T2D (Gandasi et al., 2018); however direct measures of insulin granule formation in
81 T2D have been lacking.

82

83 Insulin is initially synthesized as the prohormone precursor, proinsulin, which is folded via the
84 assistance of ER resident chaperones, such as BiP (Arunagiri et al., 2018) and GRP94 (Ghiasi et
85 al., 2019; Kim et al., 2018), while protein disulfide isomerases (PDIs), including Pdia1 and
86 Prdx4, facilitate formation of the three critical disulfide bonds necessary for mature insulin
87 structure (Jang et al., 2019; Tran et al., 2020; Winter et al., 2002). To maintain PDIs for
88 sequential rounds of disulfide bond isomerization, reducing equivalents in the form of
89 glutathione and/or thioredoxin act as the final electron donors (Birk et al., 2013; Ellgaard et al.,
90 2018), which are recycled by NADPH-dependent enzymes, glutathione reductase and

91 thioredoxin reductase, respectively. While the mechanisms regulating transfer of reducing
92 equivalents from the cytosol to the ER lumen is not well understood (Cao et al., 2020; Ellgaard
93 et al., 2018), recent studies in hepatocytes demonstrate that enhanced TCA cycle flux, which
94 increases NADPH production and glutathione reducing equivalents (GSH), results in a more
95 reduced ER environment (Gansemer et al., 2020). Conversely, diminished TCA metabolism and
96 NADPH production leads to a decrease in available GSH and a more oxidized ER lumen. In β-
97 cells, NADPH and glutathione redox fluctuate with physiological changes in glucose metabolism
98 (Ivarsson et al., 2005; Reinbothe et al., 2009). Thus, defects in mitochondrial metabolism in
99 T2D could directly alter β-cell ER redox poise through changes in cellular redox flux and
100 thereby impact proinsulin folding and downstream insulin granule production. Indeed, recent
101 work in human and rodent T2D β-cells has identified the formation of oligomeric aggregates of
102 proinsulin arising from mis-matched intermolecular disulfide bonds (Arunagiri et al., 2019; Tran
103 et al., 2020), suggesting that defects in proinsulin disulfide bond isomerization may be prominent
104 in T2D. While previous studies have demonstrated a role for NADPH and redox intermediates
105 in the regulation of insulin exocytosis (Ferdaoussi et al., 2015; Ivarsson et al., 2005; Reinbothe et
106 al., 2009; Ronnebaum et al., 2006), the contribution of redox biology to ER function and
107 proinsulin trafficking in the β-cell has not been investigated.

108

109 In the present study, we evaluated proinsulin trafficking and insulin granule formation in rodent
110 and cell culture models of hyperglycemia and T2D. Using a fluorescent pulse-chase proinsulin
111 reporter in diabetes models, we found a significant decrease in the production of insulin granules,
112 which exhibited delayed trafficking to the plasma membrane. Using APEX2 proximity labeling
113 to identify protein interactions with proinsulin, we found a profound increase in the enrichment

114 of proinsulin interactions with ER oxidoreductases in β-cells cultured under hyperglycemic-like
115 conditions, which was accompanied by diminished mitochondrial function and increased
116 glutathione oxidation. Furthermore, we directly demonstrate a significant delay in proinsulin
117 export from the ER in both animal and cell culture models of T2D, which can be regulated by the
118 availability of NADPH and cellular reducing equivalents. Together, our data suggest that
119 mitochondrial metabolism fails to maintain NADPH-derived reducing equivalents necessary to
120 support ER function in T2D β-cells, which ultimately leads to a decline in insulin granule
121 formation.

122

123 **Results**

124 **Impaired proinsulin trafficking occurs in models of β-cell dysfunction**

125 In T2D, β-cell dysfunction is accompanied by a decline in insulin-containing secretory granules
126 (Alarcon et al., 2016; Like and Chick, 1970; Masini et al., 2012). Whether alterations to insulin
127 granule formation contribute to this deficit is not known. To address this, we evaluated
128 proinsulin trafficking and insulin granule formation in a rodent diabetes model. For these
129 studies, C57BL6/J mice were placed on a Western diet (WD; 40% fat/kcal, 43%
130 carbohydrate/kcal) or standard chow (SC) for up to 8 weeks. Increased body weight (Figure 1A)
131 and *ad lib* fed hyperglycemia (Figure 1B) were apparent within 4 weeks of dietary intervention
132 and persistent for the duration of diet. Reduced glucose tolerance (Figure 1C), fasting
133 hyperinsulinemia, and impaired glucose-stimulated insulin release (Figure 1D) were observed by
134 8 weeks of WD. Collectively, these effects are consistent with defects in β-cell function in T2D
135 (Halban et al., 2014; Kahn et al., 2009).

136

137 We previously developed an *in situ* pulse-chase fluorescent-labeling strategy based on the
138 modified DNA repair enzyme, SNAPtag, to track nascent proinsulin transit through the secretory
139 system and measure insulin granule formation (Bearrows et al., 2019). We inserted SNAPtag
140 within the C-peptide region of human preproinsulin (Figure 1E), termed proCpepSNAP, and
141 demonstrated that the trafficking, processing, and secretion of proCpepSNAP/CpepSNAP are
142 consistent with the regulation of endogenous proinsulin/insulin (Bearrows et al., 2019). In this
143 system, SNAP-tag labeling is a terminal event; once labeled, the reactive cysteine is not available
144 for subsequent labeling. Taking advantage of this, proCpepSNAP expressing cells are initially

145 pre-labeled with a non-fluorescent SNAP-tag probe to mask the existing pool of (pro)CpepSNAP
146 (Figures 1F and S1). This is followed by a recovery time to allow *de novo* protein synthesis of
147 proCpepSNAP, followed by a pulse of fluorescent (SNAP-505) labeling. A subsequent 2 h
148 chase in media allows our analysis to focus on Golgi exit and insulin granule formation
149 (Bearrows et al., 2019). In the present study, islets were isolated from SC and WD fed mice and
150 treated with recombinant adenovirus expressing proCpepSNAP under control of the rat insulin
151 promoter (RIP) to ensure β-cell specific expression. Following pulse-chase labeling, we
152 observed the appearance of numerous nascent proinsulin (proCpepSNAP)-containing granules
153 throughout the cell body in primary β-cells from non-diabetic, SC fed animals (Figure 1G). In
154 contrast, β-cells from WD fed animals displayed a substantial reduction in the total number of
155 nascent, proCpepSNAP-labeled granules formed (Figure 1G, H). Moreover, distance
156 quantitation of these data revealed a significant increase in the frequency of nascent proinsulin
157 granules within 0.5 µm of the Golgi (GM130 marker) and a decrease in granules greater than 2
158 µm from the Golgi in β-cells from WD compared to SC fed mice (Figure 1I). Furthermore,
159 analysis by TIRF microscopy demonstrated a substantial decrease in the number of nascent
160 (proCpepSNAP-labeled) granules trafficking to the plasma membrane ($\leq$ 150 nm) in the WD
161 model (Figure 1J, K). Together, these data formally demonstrate an impairment in insulin
162 granule formation and trafficking in a rodent model of diet-induced diabetes, consistent with past
163 reports of reduced numbers of mature insulin granules in T2D (Like and Chick, 1970; Masini et
164 al., 2012).

165

166 To further investigate alterations to insulin granule formation, we examined islets isolated from
167 overtly diabetic C57BLKS/J-db/db mice compared to normoglycemic C57BLKS/J-db/+ controls,

168 which displayed a profound impairment in glucose tolerance (Figure 2A) accompanied by the
169 loss of glucose-regulated insulin secretion (Figure 2B). In this model, we observed significant
170 decreases in the expression of granule markers, PC2 and CPE, in islets from diabetic db/db mice
171 compared to non-diabetic db/+ controls (Figure 2C, D), consistent with previous reports (Kang et
172 al., 2019). Next, we examined an insulinoma cell culture model of β-cell dysfunction. In these
173 studies, 832/3 cells were cultured with either BSA alone or an oleate/palmitate mixture
174 conjugated to BSA (1 mM; OP) at either normal (7.5 mM) or elevated (20 mM) glucose.
175 Following 72 h culture, we measured insulin secretion after 1 h static incubation at basal (2.5
176 mM) and stimulatory (12 mM) glucose. We observed no effect of fatty acid treatment alone
177 (OP) on β-cell function, whereas elevated glucose culture alone resulted in increased basal
178 insulin secretion. In contrast, oleate/palmitate and elevated glucose together (OPG) resulted in
179 both increased basal insulin secretion and impaired glucose-stimulated insulin secretion (Figure
180 2E). By immunoblot, we observed a decrease in the expression of granule markers, PC2 and
181 CPE, in OPG-cultured 832/3 cells compared to BSA controls, whereas another key granule
182 protein, CgB, was unaffected (Figure 2F, G). Using our fluorescent pulse-chase proCpepSNAP
183 reporter system, we demonstrate that OPG-cultured 832/3 cells displayed increased retention of
184 nascent proinsulin-containing (proCpepSNAP-labeled) granules proximal to the Golgi (less than
185 3 μm) and decreased numbers of granules distal to the Golgi (greater than 5 μm; Figure 2H, I),
186 similar to β-cells from WD mice (Figure 1I). Additional analysis by TIRF microscopy
187 confirmed the decrease in nascent insulin granules reaching the plasma membrane after a 4 h
188 chase in 832/3 cells cultured under high glucose (HG; 20 mM) compared to normal glucose (NG;
189 7.5 mM) conditions (Figure 2J, K). Following a prolonged chase (> 18 h), we observed a similar
190 number of nascent granules (proCpepSNAP-labeled) in the BSA (control) and OPG-cultured

191 cells (Figure 2L, M), suggesting that defects in insulin granule formation in our OPG model
192 stemmed from trafficking delays, rather than reduced expression and/or stability of our reporter.
193 Last, we examined total insulin granules by density sedimentation in control (BSA) and OPG-
194 cultured 832/3 cells. Here, we observed a significant shift of insulin-containing granules to
195 lighter density fractions from OPG cultured cells, suggesting there was an alteration to granule
196 composition (Figure 2N). Collectively, these data demonstrate impairments in insulin granule
197 formation and alterations to granule composition in both cell culture and animal models of β-cell
198 dysfunction.

199

200 **Proximity labeling of the proinsulin interactome reveals an ER export delay**

201 We hypothesized that changes in the proteins interacting with proinsulin along the secretory
202 pathway contribute to the decrease in formation of insulin secretory granules. To address this,
203 we used an *in situ* proximity labeling strategy to systematically map the proinsulin interactome
204 via the engineered ascorbate peroxidase, APEX2, inserted within the C-peptide region of human
205 preproinsulin (proCpepAPEX2), which is analogous to our proCpepSNAP construct. In the
206 presence of hydrogen peroxide, APEX2 generates a short-lived (<1 ms), membrane
207 impermeable, biotin-phenoxy radical that biotinylates neighboring proteins *in situ* within a small
208 labeling radius (20 nm; labeling time < 1 min) allowing us to capture transient protein
209 interactions that are difficult to monitor with traditional approaches (Hung et al., 2016; Lam et
210 al., 2015). Initial validation studies demonstrated that the expression of V5-tagged
211 proCpepAPEX2 in 832/3 cells co-localized with insulin by immunostaining (Figure 3A).
212 Furthermore, we observed substrate-dependent (biotin-phenol and hydrogen peroxide)

213 biotinylation of putative proinsulin-interacting proteins identified with a fluorescent streptavidin
214 probe (Figure 3B; endogenous biotin-containing carboxylases are detected independent of
215 APEX2 labeling). Affinity purification of proCpepAPEX2 biotinylated proteins (Figure 3C)
216 revealed interactions with the ER resident chaperone, GRP94, and granin protein, CgB, (Figure
217 S2A) which have both been demonstrated to regulate proinsulin trafficking (Bearrows et al.,
218 2019; Ghiasi et al., 2019; Kim et al., 2018). In contrast, no labeling of the plasma membrane
219 SNARE, syntaxin-4, was observed, as expected (Figure S2A).

220

221 Using the proximity labeling system, we identified proinsulin-interacting proteins by quantitative
222 proteomics. We first compared peroxide (APEX2 dependent labeling) to non-peroxide (APEX2
223 independent labeling) treatments (Figure 3C) and identified 74 proteins with greater than 1.2-
224 fold enrichment, which we categorized by their subcellular locations (Figure 3D, E). As
225 expected, numerous ER resident chaperones (Hspa5, Hsp90b1), ER oxidoreductases
226 (Pdia1/P4hb, Prdx4), and secretory granule proteins (CgB, Vgf) were observed to interact with
227 proinsulin, which have all been previously demonstrated to regulate proinsulin folding
228 (Arunagiri et al., 2018; Ghiasi et al., 2019; Jang et al., 2019; Kim et al., 2018; Tran et al., 2020;
229 Winter et al., 2002) and trafficking (Bearrows et al., 2019; Stephens et al., 2017). We next
230 examined changes in the proinsulin interactome in 832/3 cells cultured with elevated glucose and
231 fatty acids (OPG) compared to control (BSA) cells (Figure 3F). Analysis by subcellular location
232 revealed a selective increase in proinsulin interactions with ER resident proteins and a
233 corresponding decrease in interactions with proteins residing in more distal secretory
234 compartments (Golgi, secretory granule) (Figure 3G, H). Enriched interactions with the majority
235 of ER proteins, such as BiP (Hspa5) and GRP94 (Hsp90b1), occurred independent of changes in

236 gene expression (Figure 4A-C), whereas a subset of ER oxidoreductases, including Txndc12 and
237 Prdx4, were modestly upregulated (Figure 4C). Similarly, decreased interactions with various
238 secretory proteins, such as TMED9, TMED10, and CgB, were not accompanied by changes in
239 protein expression (Figure 4A, B and 2F, G).

240

241 Based on our observation of increased interactions of proinsulin with ER proteins in a model of
242 β-cell dysfunction, we hypothesized that ER export of proinsulin is delayed, which leads to
243 impairments in insulin granule formation. To test this, we modified our pulse-chase labeling
244 protocol to capture early-stage transit of proinsulin from the ER to Golgi (Figure S1B) using
245 GRP94 and TGN38 immunostaining to demarcate the ER and Golgi, respectively. As expected,
246 examination of control (BSA-cultured) cells demonstrated successful trafficking of newly
247 synthesized proinsulin (proCpepSNAP) to the Golgi, which was largely absent from the ER
248 (Figure 4D). In contrast, pulse-chase labeling in OPG-cultured β-cells revealed a substantial
249 retention of nascent proinsulin coincident with the ER and very little detection within the Golgi.
250 Quantitation revealed a significant decrease in the ratio of Golgi to ER proCpepSNAP
251 fluorescence intensity in OPG-cultured cells (Figure 4E). We also examined ER-Golgi
252 proinsulin trafficking in β-cells from overtly diabetic C57BLKS/J-db/db mice. While β-cells
253 from normoglycemic db/+ controls displayed the expected trafficking of newly synthesized
254 proinsulin (proCpepSNAP) from the ER (GRP94) to the Golgi (GM130), we observed a
255 substantial retention of nascent proinsulin within the ER in β-cells from db/db diabetic mice
256 (Figure 4F) with a significant decrease in the Golgi to ER proCpepSNAP fluorescence (Figure
257 4G).

258

259 The accumulation of proinsulin within the ER could stem from activation of the ER stress
260 response, which has been suggested to contribute to the development of β-cell dysfunction in
261 T2D (Yong et al., 2021). While expansion of ER membranes has been demonstrated in both
262 human and rodent T2D β-cells (Alarcon et al., 2016; Boland et al., 2017; Marchetti et al., 2007;
263 Masini et al., 2012); dilation of the ER lumen, which is a key hallmark of proteotoxic stress, is
264 not commonly observed. Consistent with these latter data, the increased retention of nascent
265 proinsulin in the ER was not accompanied by distension of the ER lumen or other changes in ER
266 ultrastructure in β-cells from diabetic db/db mice (Figure 5A). In 832/3 cells cultured with fatty
267 acid alone (OP) or fatty acid plus elevated glucose (OPG), we failed to detect upregulation of ER
268 stress markers, ATF4, CHOP, XBP-1(s/u), GADD34 or BiP by qRT-PCR as compared to
269 thapsigargin-treated cells (Figure 5B). Similarly, expression of CHOP and cleaved caspase 3 by
270 immunoblot were not detected under OPG culture conditions (Figure S3A). Furthermore, pulse-
271 chase analysis using our fluorescent proCpepSNAP reporter revealed that the chemical
272 chaperone, TUDCA, which has been used to ameliorate ER stress (Ozcan et al., 2006), could not
273 rescue the proinsulin ER export delay observed in OPG-cultured 832/3 cells (Figure S3B).

274

275 To examine if the ER export delay was specific to proinsulin or instead was a general defect in
276 ER protein export, we examined ER-Golgi trafficking of another granule protein, CgB, using an
277 analogous pulse-chase system, CLIPtag. Notably, CLIPtag uses a distinct substrate from
278 SNAPtag allowing us to perform dual pulse-chase studies of both proteins in the same cell
279 (Gautier et al., 2008). We generated a C-terminal CLIP-tagged CgB reporter, which was

280 expressed at levels similar to endogenous CgB (Figure 5C) and co-trafficked with proCpepSNAP
281 into punctate structures following a 2 h pulse-chase (Fig 5D), likely representing maturing
282 insulin granules. Using this dual pulse-chase system to examine ER-Golgi trafficking (Figure
283 S1), we demonstrate that in BSA-cultured (control) 832/3 cells, nascent proinsulin
284 (proCpepSNAP) and CgB (CgB-CLIP) similarly trafficked to the Golgi following pulse-chase
285 labeling (Figure 5E, F). In OPG-cultured 832/3 cells, CgB-CLIP trafficking from the ER to
286 Golgi occurred without delay and mirrored control (BSA) cells (Figure 5E) with similar co-
287 localization to the Golgi marker, TGN38 (Figure 5F). This was in stark contrast to proinsulin,
288 which was retained in the ER in OPG-cultured 832/3 cells (Figure 5E), displaying reduced co-
289 localization with both CgB-CLIP (Figure 5G) and the Golgi marker TGN38 (Figure 5F).
290 Collectively, these data demonstrate a specific delay in ER export of proinsulin accompanying
291 chronic exposure to hyperglycemic and hyperlipidemic-like conditions, which is independent of
292 overt ER stress or a general impairment in ER protein export.

293

294 **Metabolic regulation of ER redox homeostasis**

295 In hepatocytes, mitochondrial activity can directly influence ER redox homeostasis via the
296 generation of glutathione (GSH) reducing equivalents (Gansemer et al., 2020). Whether a
297 similar link exists in β-cells is not known, but alterations in ER redox poise could explain the
298 defects in ER export of proinsulin in diabetes models. To test this, we first examined
299 mitochondrial function in control (BSA) and OPG-cultured 832/3 cells and demonstrate a
300 significant decrease in overall mitochondrial oxidative consumption (Figure 6A), including a
301 decrease in basal respiration (Figure S4A), maximum respiration (Figure S4B), and ATP

302 production (Figure S4C), consistent with past reports (Haythorne et al., 2019). Furthermore,
303 decreased mitochondrial function coincided with a corresponding shift in the redox balance of
304 glutathione to the oxidized state (GSSG; Figure 6B) that was not simply due to an increase in the
305 production of reactive oxygen species (Figure 6C). Because reduced glutathione (GSH) can be a
306 final electron donor for PDIs regulating disulfide bond isomerization (Birk et al., 2013; Ellgaard
307 et al., 2018), we reasoned that the decrease in GSH may limit proinsulin disulfide bond
308 formation leading to an ER export delay as previously suggested (Arunagiri et al., 2019; Tran et
309 al., 2020). To test this, we examined if addition of chemical reducing equivalents, DTT, could
310 rescue the proinsulin trafficking delay in OPG-cultured β-cells. Note that the concentration of
311 DTT (0.5 mM) used did not impact β-cell function following overnight exposure (Figure S4D),
312 but did lower the GSSG/GSH ratio (Figure S4E). In control (BSA cultured) cells, acute addition
313 of DTT (4 h) had no discernible impact on ER to Golgi trafficking of newly synthesized,
314 proCpepSNAP-labeled, proinsulin as compared to the vehicle control (Figures 6D, E and S4F).
315 In contrast, DTT treatment restored ER to Golgi proinsulin trafficking in OPG-cultured β-cells.
316 These data suggest that OPG culture can lead to an insufficient supply of reducing equivalents
317 necessary to maintain efficient ER export of proinsulin (Figure 6F).

318

319 Cellular reducing equivalents, such as GSH, are re-generated by NADPH-dependent enzymes.
320 Based on this, we reasoned that NADPH production may be necessary to support ER functions,
321 such as proinsulin disulfide bond formation and export, via supplying cellular (GSH) reducing
322 equivalents (Figure 7A) as previously suggested (Gansemer et al., 2020). To test this, islets were
323 treated with recombinant adenovirus expressing either a non-targeting control shRNA (SAFE) or
324 an shRNA targeting Idh1, the major cytosolic NADPH-producing enzyme in β-cells, which has

325 been previously shown to support insulin granule exocytosis (Bauchle et al., 2021; Ferdaoussi et
326 al., 2015; Ronnebaum et al., 2006). Note that Idh1 loss does not impair mitochondrial function
327 (Ronnebaum et al., 2006). By qRT-PCR, we observed a strong suppression of Idh1 (Figure 7B).
328 Importantly, our viral backbone co-expresses mCherry from a separate RNA pol II promoter
329 (PGK) allowing the specific identification of transduced (Idh1 or SAFE shRNA) islet cells
330 (Bearrows et al., 2019). Using this system, we examined insulin granule formation via
331 fluorescent pulse-chase labeling of our proCpepSNAP reporter, which is under control of the rat
332 insulin promoter (RIP), such that mCherry+ proCpepSNAP+ cells correspond to Idh1
333 knockdown β-cells (Figure S5). Here, we observed a substantial (> 50%) decrease in the
334 production of nascent (proCpepSNAP-labeled) insulin granules in Idh1 knockdown compared to
335 control (SAFE) β-cells (Figure 7C, D). Next, we examined whether DTT addition could
336 replenish necessary reducing equivalents and thereby restore the deficit in insulin granule
337 formation in Idh1 knockdown β-cells (Figure 7A). Prior to pulse-chase labeling, mouse islets
338 were treated with 0.5 mM DTT (or vehicle control) for 4 h. Consistent with our previous data
339 (Figure 6D, E), addition of DTT, compared to vehicle control, did not affect insulin granule
340 formation in Ad-shRNA-SAFE treated control cells (Figure 7E, F). In contrast, pre-treatment of
341 Idh1 shRNA KD β-cells with DTT rescued insulin granule formation, restoring the levels to the
342 Ad-shRNA control. Collectively, our data demonstrate that proinsulin trafficking and insulin
343 granule formation can be regulated by NADPH production and reducing equivalent availability
344 (Figure 7A) and highlight a direct link between mitochondrial and secretory dysfunction in the
345 decline of β-cell function in T2D.

346

347 **Discussion**

348 Defects in the β-cell's secretory pathway, including changes to insulin trafficking, reduced
349 insulin storage, impaired proinsulin processing, and hyperproinsulinemia, have been known for
350 decades to occur in T2D (Alarcon et al., 2016; Halban et al., 2014; Kahn et al., 2009; Kahn and
351 Halban, 1997; Like and Chick, 1970; Masini et al., 2012; Ward et al., 1984). Increased
352 exocytosis of immature granules (Rhodes and Alarcon, 1994) as well as enhanced degradation of
353 newly synthesized insulin granules in T2D (Pasquier et al., 2019; Shrestha et al., 2020)
354 contribute to the overall decrease in insulin storage and hyperproinsulinemia; however, the
355 underlying mechanisms for these defects are poorly understood and the links to overnutrition and
356 hyperglycemia remain vague. Our study focuses on an emerging concept that oxidative protein
357 folding in the ER is perturbed in the pathogenesis of β-cell dysfunction (Arunagiri et al., 2019;
358 Jang et al., 2019; Tran et al., 2020) and we link this defect to the loss of insulin granules. We
359 show that changes in cellular redox homeostasis delay proinsulin export from the ER leading to
360 decreased insulin granule formation in animal and cell culture models of overnutrition and
361 diabetes. Furthermore, we demonstrate that ER export of proinsulin can be regulated by
362 NADPH and reducing equivalent availability. Loss of the NADPH-producing enzyme, Idh1,
363 compromises insulin granule formation, while addition of chemical reducing equivalents can
364 restore insulin granule production. Collectively, our data highlight a direct link between nutrient
365 metabolism and the β-cell's secretory pathway as a critical node in the regulation of insulin
366 biosynthesis (Figure 8)

367

368 Following the emergence of nascent proteins from the ER protein-conducting channel, Sec61,
369 disulfide bonds readily form in the oxidizing environment of the ER lumen. In the case of
370 disulfides arising from non-sequential cysteine residues, such as the three disulfide bonds in
371 proinsulin, rearrangement of mis-paired disulfides requires reduction via PDIs and subsequent
372 re-oxidation of cysteine thiols to form the correct disulfide linkages (Ellgaard et al., 2018; Winter
373 et al., 2002). Using our proximity labeling system, we identified 11 ER oxidoreductases,
374 including Prdx4 and Pdia1, that interact with proinsulin under normal physiological conditions,
375 highlighting a potential critical role for disulfide bond isomerization in proinsulin folding.
376 Following chronic exposure to hyperglycemic and hyperlipidemic-like conditions, we observed a
377 significant elevation in the interactions between proinsulin and ER oxidoreductases, which has
378 been previously reported in human T2D β-cells (Tran et al., 2020). This increase in proinsulin
379 interactions with ER oxidoreductases may be driven by the aberrant formation of mis-paired
380 intermolecular disulfide bonds between proinsulin molecules (Arunagiri et al., 2019; Tran et al.,
381 2020) and lead to the ER export delay reported here. Based on these data, we propose that the
382 ER lumen becomes hyperoxidizing during the pathogenesis of β-cell dysfunction, which impedes
383 the necessary re-shuttling of proinsulin's disulfide linkages and thereby delays ER export of
384 proinsulin (Figure 8). In support of this mechanism, the delay in ER export can be reversed by
385 the addition of chemical reducing equivalents, suggesting that proinsulin disulfide bond
386 isomerization is a kinetic determinant in proinsulin export from the ER. Similarly, antioxidant
387 treatment has been shown to decrease ER stress and attenuate β-cell dysfunction and diabetes
388 onset in genetic mouse models of ER dysfunction (Han et al., 2015; Hassler et al., 2015;
389 Malhotra et al., 2008). Interestingly, we observed no defect in ER to Golgi transit of CgB, which
390 contains a single pair of sequential cysteines forming its lone disulfide linkage. Thus, CgB may

391 be less dependent on reducing equivalents for correct disulfide bond formation and ER export.
392 Together, our data provide compelling evidence linking defects in oxidative protein folding in
393 the ER to a decrease in insulin granule formation via delayed ER export of proinsulin during the
394 progression of β-cell dysfunction in T2D (Figure 8).

395

396 Recent data demonstrates that ER oxidative protein folding can be regulated via nutrient
397 metabolism (Gansemer et al., 2020) through NAPDH dependent recycling of redox
398 intermediates, glutathione and/or thioredoxin, which are necessary to reset PDIs for sequential
399 rounds of client protein disulfide bond isomerization (Birk et al., 2013; Ellgaard et al., 2018).
400 Distinct from other cell types, the β-cell is uniquely positioned to sense physiological
401 fluctuations in glucose via the generation of metabolic signals (Boland et al., 2017). Here, we
402 speculate that nutrient metabolism in the β-cell is directly coupled to secretory function through
403 the regulation of ER redox poise. In this pathway, a rise in glucose metabolism, which increases
404 preproinsulin mRNA translation (Wicksteed et al., 2003), also supplies reducing equivalents to
405 facilitate proinsulin disulfide bond isomerization in the ER and thereby expedite proinsulin
406 biosynthesis and insulin production. In support of this, loss of glucose-dependent NADPH
407 production via Idh1 suppression impairs insulin granule formation, which can be restored via
408 replacement of cellular reducing equivalents. During the pathogenesis of T2D, chronic exposure
409 to nutrient excess and hyperglycemia has the unfortunate consequence of impairing
410 mitochondrial function[45] resulting in diminished production of NADPH and glutathione/
411 thioredoxin reducing equivalents (Ferdaoussi et al., 2015), which are necessary for ER function
412 (Birk et al., 2013; Ellgaard et al., 2018). As a result, the ER lumenal environment falters in
413 efficient proinsulin disulfide bond isomerization leading to the formation of proinsulin

414 aggregates (Arunagiri et al., 2019; Tran et al., 2020), which may trigger ERAD and other
415 degradative pathways (Pasquier et al., 2019; Shrestha et al., 2020, p. 1), and ultimately decrease
416 insulin granule formation. While we failed to detect increased levels of cellular ROS, we cannot
417 rule out the possibility that a portion of the reduced glutathione pool, was consumed to buffer
418 accumulating ROS and thereby lead to a decrease in GSH available for proinsulin disulfide bond
419 isomerization. Similarly, the limited supply of NADPH could stem directly from decreased
420 mitochondrial output of necessary substrates such as citrate/isocitrate and/or increased utilization
421 by NADPH oxidases to elevate cytosolic (and possibly ER) levels of hydrogen peroxide. Based
422 on these possibilities, future studies examining the mechanisms intertwining β-cell nutrient
423 metabolism and secretory function may offer unique insight into novel pathways that could be
424 exploited for diabetes treatment.

425

426 Numerous studies have demonstrated that induction of ER stress can perturb β-cell function and
427 may contribute to the development of β-cell dysfunction in T2D (Yong et al., 2021). Loss of
428 critical ER stress response sensors, such as PERK and Ire1α, can sensitize β-cells to nutrient
429 stresses and/or directly impair β-cell function leading to the development of diabetes (Delépine
430 et al., 2000, p. 2; Harding et al., 2001; Hassler et al., 2015; Xu et al., 2014). Similarly, loss of
431 the ER chaperone, GRP94, the BiP co-chaperone, $p58^{IPK}$, and PDIs, Pdia1 and Prdx4,
432 compromise proinsulin folding, resulting in ER stress and loss of insulin content (Ghiasi et al.,
433 2019; Jang et al., 2019; Kim et al., 2018, p. 94). In humans, monogenic forms of diabetes arising
434 from *INS* mutations can prevent proper proinsulin disulfide bond formation acting as dominant
435 negative suppressors of wild type proinsulin trafficking (Haataja et al., 2021; Liu et al., 2007;
436 Støy et al., 2010). While these studies demonstrate that perturbations in ER functions and

437 proinsulin folding can compromise β-cell health and insulin production, direct evidence for ER
438 stress as a causative feature in the development of T2D is less clear (Alarcon et al., 2016;
439 Marchetti et al., 2007). Increased PERK and Ire1α activity have been described in pre-diabetic
440 β-cells (Engin et al., 2014; Lipson et al., 2006; Yong et al., 2021), yet diminished, rather than
441 increased, expression of ATF6 and XBP-1(s) occur in β-cells from humans with long-standing
442 T2D (Engin et al., 2014). Moreover, human β-cells are known to cycle between varying levels
443 of UPR protein expression (Xin et al., 2018), which may represent the natural β-cell adaptation
444 to changes in nutrient load. Indeed, activation of the ER stress pathway is necessary for the β-
445 cell proliferative response to diet-induced obesity (Sharma et al., 2015). Expansion of ER
446 membranes has been demonstrated in both human and rodent T2D β-cells, which may be
447 necessary to support increased proinsulin biosynthesis (Alarcon et al., 2016; Boland et al., 2017;
448 Marchetti et al., 2007; Masini et al., 2012); however distension and/or dilation of the ER lumen,
449 a classic marker of proteotoxic ER stress, is not commonly observed. Consistent with these data,
450 we failed to detect changes in ER ultrastructure in diabetic db/db mice and saw little evidence for
451 overt ER stress response activation in our cell culture model, despite clear effects on ER
452 retention of proinsulin in both models. These unresolved issues encourage continued
453 investigation in defining how physiological stresses manifest in the β-cell and determining when
454 the adaptive responses become insufficient to mitigate cellular damage and/or become
455 maladaptive.

456

457 **Materials and methods**

458 **Cell culture, islet isolation, and reagents**

459 832/3 cells (a kind gift from Dr. Christopher Newgard) were cultured as previously described
460 (Hohmeier et al., 2000). 832/3 cells stably expressing proCpepSNAP have been described
461 previously (Bearrows et al., 2019). For introduction of adenoviral reporters, cells were
462 transduced with ~1-5 x 10^7 IFU/ mL adenovirus for 18 h and assayed 72-96 h post-treatment.
463 Cell culture reagents were from Thermo Life Technologies unless specified otherwise. Chemical
464 reagents were from Sigma-Aldrich unless specified otherwise. BSA-conjugated fatty acid
465 solution was prepared as follows: Oleate/palmitate (2:1; 10 mM) was dissolved in water at 95^0C,
466 cooled to 50^0C, BSA (Sigma, fatty acid free) added to a final concentration of 10%, and
467 maintained at 37^0C for an additional 1 h. Mouse islets were isolated via collagenase V digestion
468 and purified using Histopaque 1077 and 1119. Islets were cultured in RPMI supplemented with
469 10% fetal bovine serum and 1 % penicillin and streptomycin and maintained at 37°C in 5% CO_2.
470 Pools of islets were transduced with ~1-5 x 10^8 IFU/ mL adenovirus for 18 h and assayed 72-96
471 h post-treatment.

472

473 **Animal studies**

474 Male C57BL6/J mice (8-10 wk old; Jackson Laboratories) were placed on a Western diet
475 (Research Diets, D12079B) or standard chow for up to 14 weeks. Body weight and *ad lib* fed
476 blood glucose were measured weekly. BKS.Cg-Dock7^m (C57BLKS/J) Lepr$^{db/+}$ and Lepr$^{db/db}$
477 mice (db/+, db/db) were either generated by heterozygous cross and genotypes confirmed via
478 real time PCR according to Jackson Laboratories or directly purchased from Jackson

479 Laboratories. Hyperglycemic db/db mice (*ad* lib fed blood glucose > 220 mg/dl) were compared
480 to age-matched (10-14 weeks old), normoglycemic littermate controls (db/+). Glucose tolerance
481 was measured in 4-6 hr fasted mice given a 1 mg/ g body weight glucose (i.p.) challenge. Blood
482 glucose was determined using a One Touch Ultra 2 glucometer. Plasma insulin was determined
483 by ELISA (ALPCO). All animal protocols were approved by the University of Iowa
484 Institutional Animal Use and Care Committee

485

486 **Plasmids and viruses**

487 The shuttle plasmid, pENTR-RIP, containing a rat insulin promoter (RIP), multiple cloning site,
488 chloramphenicol resistance marker, ccdB, and a bovine growth hormone (bGH) polyA signal
489 was generated by Gibson assembly (IDT) and subcloned into pENTR2b (Thermo Life) replacing
490 the entire cassette between the attP1 and attP2 sites. V5-tagged APEX2 was inserted near the
491 ApaI site of human preproinsulin via gblock synthesis (IDT) and subcloned into pENTR-RIP via
492 Gibson assembly. PCR fragments of CgB (DNASU) and CLIP (gift from Eric Campeau;
493 RRID:Addgene_29650) were subcloned into pENTR-RIP via Gibson assembly. RIP-proCpep-
494 APEX2 and RIP-CgB-CLIP were assembled into a modified pAd-PL/DEST via Gateway
495 cloning using LR Clonase II. Adenovirus containing rat insulin promoter (RIP) expressing
496 Grx1-GFP2 was a kind gift from A. Linneman, Indiana University School of Medicine (Reissaus
497 et al., 2019). Adenoviruses expressing shRNA targeting mouse Idh1 (AdU6-Idh1 shRNA-PGK-
498 mCherry) and non-targeting control shRNA (AdU6-SAFE-shRNA-PGK-mCherry) have been
499 described previously (Bauchle et al., 2021). Recombinant adenoviruses were generated in

500 HEK293 cells and purified by cesium chloride gradient. All sequences were verified by the Iowa
501 Institute of Human Genetics, University of Iowa.

502

503 **Glucose-stimulated insulin secretion**

504 Insulin secretion was measured by static incubation as previously described (Stephens et al.,
505 2017). Cells were lysed in RIPA buffer and total protein determined by BCA (Pierce). Insulin
506 (secreted and content) was measured by ELISA (rodent 80-INSMR-CH10; ALPCO) or Alphalisa
507 (AL204C; Perkin-Elmer Insulin).

508

509 **Immunoblot analysis**

510 Clarified cell lysates were resolved on 4-12% NuPAGE gels (Thermo Life Technologies) and
511 transferred to supported nitrocellulose membranes (BioRad). Membranes were probed with
512 diluted antibodies raised against chromogranin B (goat, Santa Cruz C-19 1:1000), CHOP
513 (mouse, 1:1000 Cell Signaling 2895), cleaved Caspase 3 (rabbit, R&D systems MAB835,
514 1:500), CPE (rabbit, Proteintech 13710-1-AP, 1:1000), GRP94 (rabbit, kind gift of Dr.
515 Christopher Nicchitta, Duke University, 1:5000), PC2 (rabbit, Proteintech 10552-1-AP, 1:1000),
516 proinsulin (mouse, Iowa Developmental Studies Hybridoma Bank GS-98A, 1:500), syntaxin-4
517 (rabbit, Millipore AB5330, 1:1000), TMED9 (rabbit, Proteintech 21620-1-AP, 1:10,000),
518 TMED10 (rabbit, Bethyl Laboratories, A305-219A, 1:1000), gamma-tubulin (mouse, Sigma
519 T5326, 1:10,000). Donkey anti-mouse, anti-rabbit, or anti-goat antibodies (Licor) coupled to IR-
520 dye 680 or 800 were used to detect primary antibodies. Streptavidin-conjugated to IR dye 680

521 (1:1000, Thermo) was used to detect biotinylated proteins. Blots were developed using an
522 Odyssey CLx Licor Instrument.

523

524 **Fluorescence microscopy and imaging**

525 Isolated islets expressing proCpepSNAP (AdRIP) were dispersed into monolayers using
526 Accutase (Sigma-Aldrich) and plated onto HTB9 coated coverslips or 6 cm glass bottom dishes
527 (Mattek) as previously described (Bearrows et al., 2019; Hayes et al., 2017). 832/3 cells stably
528 expressing proCpepSNAP were plated on HTB9 coated coverslips at low density and cultured
529 overnight as previously described (Bearrows et al., 2019). For SNAPtag labeling, cells were
530 initially incubated with SNAPcell block (10 μM; NEB) diluted in culture media for 20 min,
531 washed 3 times for 5 min each. To allow for *de novo* protein synthesis of new proCpepSNAP,
532 cells were cultured for an additional 2 h in experiments examining post-Golgi granule formation
533 or 45 min in experiments examining ER-Golgi transport. Cells were pulse-labeled with
534 SNAPcell-505 (1 μM; NEB) for 20 min in media, washed 3 times for 5 min each in culture
535 media with glucose (5 mM) and chased as indicated. For studies utilizing CgB-CLIP, an
536 identical labeling scheme was followed using CLIPcell block (10 μM; NEB) and CLIPcell-TMR
537 (1 μM; NEB) where appropriate. Following treatments, cells were fixed in 10 % neutral-
538 buffered formalin. For immunostaining, cells were incubated overnight with antibodies raised
539 against GM130 (mouse, BD Transduction 610823, 1:200), GRP94 (rabbit, kind gift of Dr.
540 Christopher Nicchita, Duke University, 1:500), TGN38 (mouse, Novus Biologicals NB300-575,
541 1:200), or V5 epitope tag (rabbit, GeneTex GTX117997, 1:100) as indicated. Highly cross-
542 adsorbed fluorescent conjugated secondary antibodies (whole IgG, donkey anti-guinea pig-

543 AlexaFluor 488, donkey anti-rabbit rhodamine red-X, donkey anti-mouse AlexaFluor 647;
544 Jackson ImmunoResearch) were used for detection. Cells were counterstained with DAPI and
545 mounted using Fluorosave (Calbiochem). Images were captured on a Leica SP8 confocal
546 microscope using a HC PL APO CS2 63x/1.40 oil objective with 3x zoom as z-stacks (5 per set,
547 0.3 μm step, 0.88 μm optical section) and deconvolved (Huygen's Professional). Granule
548 distance measurements from the Golgi were determined using a distance transformation module
549 in Imaris (Bitplane) from spot-rendered granules (SNAP-505 labeled) and surface rendering of
550 the Golgi identified by GM130 or TGN38 immunostaining. Granule distances were binned and
551 expressed as a percentage of the total to normalize between cells. Total granule number were
552 also calculated from these studies with respect to the number of pulse-chased labeled cells. For
553 islet studies, we used a cutoff of less than 0.5 μm to identify granules proximal to the Golgi as
554 attached, and granules > 2 μm as successful Golgi export based on time course studies of granule
555 distance clustering (Bearrows et al., 2019). Golgi/ER fluorescence of SNAP labeling was
556 determined from thresholded masks defining Golgi and ER area by immunostaining using
557 macros written for Fiji NIH software. For plasma membrane detection, immunostained (fixed)
558 cells were maintained in PBS and imaged using a Leica TIRF AM microscope (100x oil
559 objective) in TIRF mode with a penetration depth of 110-150 nm. In some experiments,
560 SNAP25 immunostaining was used to define the plasma membrane. Granule numbers from
561 SNAP-labeling, cell area and or cell number (defined by nuclei) were determined by Fiji/ImageJ.

562

563 For glutathione (GSSG/GSH) redox measurements, 832/3 cells were treated with AdRIP-Grx1-
564 GFP2 and imaged on an inverted Olympus IX83 microscope with a 20x objective (HC PL APO
565 CS2; 0.75 NA) using Chroma 49002 GFP/CY2 Bandpass (470/535) and custom Chroma BX3-

566 mounted (395/510) filters. Cells were subsequently cultured and re-imaged following DTT (10
567 mM) and diamide (5 mM) treatment, for 12 min each (Bauchle et al., 2021). Fluorescent
568 intensities of each channel were calculated from masked images (to remove background) of
569 whole cells using macros written for Fiji NIH software. Ratiometric intensities (395 nm/470 nm)
570 were normalized by comparing to DTT (0%) and diamide (100%) treated samples using
571 GraphPad Prism software.

572

573 For ROS measurements, 832/3 cells were cultured in opaque HTB9-coated 96-well plates as
574 indicated. Menadione (100 μM) treatment for 1 h was used as a positive control. Cells were
575 incubated for 0.5 h with Cell ROX Deep Red (5 μM), washed, and analyzed using a Spectromax
576 MD5 plate reader.

577

578 **Ultrastructure**

579 All EM related reagents were from Electron Microscopy Sciences (EMS; Hatfield, PA). Isolated
580 islets were PBS washed and fixed in 2.5% glutaraldehyde, 4 % formaldehyde cacodylate buffer
581 overnight (16-18 h) at 4ºC. Tissue was post-fixed in 1% OsO_4 for 1 h, dehydrated using a graded
582 alcohol series followed by propylene oxide and embedded in Epon resin as previously described
583 (Joshi et al., 2014). Resin blocks were cut to ultrathin (50-70 nm) sections with a diamond knife
584 and mounted on Formvar-coated copper grids. Grids were double contrasted with 2% uranyl
585 acetate then with lead citrate. Images were captured at 1,500x, 3,000x, 6,000x, and 8,000x
586 magnifications by a JEOL JEM-1400 transmission electron microscope.

587

588 **Density gradient isolation of secretory granules**

589 Cells were collected, washed in ice-cold PBS, and disrupted using 15 strokes in a pre-chilled
590 ball-bearing cell homogenizer (Isobiotec) with a 14 µm clearance in 10 mM MES pH 6.5, 1 mM
591 MgSO4, 1 mM EDTA, 0.3 M sucrose as previously described (Bearrows et al., 2019; Stephens et
592 al., 2017). Post-nuclear supernatants were layered atop 8-23% linear iodixanol (Optiprep)
593 gradients and resolved at 110,000 x g's in an SW41 for 16-18 h. Fractions were manually
594 collected by tube puncture. Iodixanol gradients were verified by absorbance at 340 nm. Insulin
595 content was determined by ELISA (ALPCO) and normalized to the total insulin content from
596 post-nuclear supernatant.

597

598 **APEX2 biotinylation and proteomics analysis**

599 APEX2 biotinylation was performed using a modified protocol (Hung et al., 2016) as follows.
600 Cells expressing proCpepAPEX2 were cultured for 1 h in SAB containing 2.5 mM Glc followed
601 by addition of 500 µM biotin phenol (Adipogen) for 0.5 h. Diluted H_2O_2 was added to a final
602 concentration of 1 mM and incubated for 1 min. Non-peroxide-treated samples were used as
603 controls for non-enzymatic labeling such as endogenous biotin-containing proteins. Cells were
604 washed 5x in PBS containing 10 mM sodium ascorbate, 5 mM Trolox (Acros), and 10 mM
605 sodium azide for 1 min each. Cells were scraped, collected by centrifugation, and lysed in RIPA
606 containing 10 mM sodium ascorbate, 5 mM Trolox, 10 mM sodium azide, and Halt protease
607 cocktail (Thermo). For proteomics studies, cell pellets were snap frozen in a dry-ice ethanol bath
608 prior to lysis. Pierce-660 (Thermo Life) was used to determine protein concentrations. For

609 pulldowns, clarified cell lysates (1-2 mg/mL) were added to high capacity Neutravidin agarose
610 resin (Thermo Life) and rotated end over end overnight (16-18 h) at 4°C. Bound proteins were
611 washed in RIPA, 1 M KCl, 0.1 M sodium carbonate, 2 M urea in 10 mM Tris pH 8.0, RIPA
612 solution without detergent, and eluted at 70°C for 15 min in 2x LDS sample buffer (Thermo
613 Life) containing 2 mM biotin.

614

615 Proteomic analysis was performed on Neutravidin affinity-purified lysates (~1.5 mg starting
616 material) with reproducible recovery verified with 4-12% NuPAGE (Thermo Life) and silver
617 staining. Sample pre-cleaning and in-solution tryptic digestions were accomplished with a lab-
618 built silica / C-18 trapping mini-column (Zougman et al., 2014). Recovered peptides were
619 labeled by reductive amination as previously described (Yu et al., 2017) using distinct (light,
620 medium, heavy) dimethyl isotopomers (Boersema et al., 2009; Hsu et al., 2003; Yu et al., 2017).
621 Completion of labeling was confirmed by MALDI-TOF and distinct isotopomer-labeled samples
622 from each treatment were mixed at equal ratios for LC–MS/MS analysis. Rather than
623 subtracting the median ratio of spatially inaccessible false positives to normalize regional APEX,
624 heavy (+36) and light (+28) isotopes were applied in crossover to two replicates of samples
625 cultured in OPG vs BSA control. Non-peroxide treated (no APEX labeling) cells were labeled
626 with the medium isotopic channel (+32). Mass spectrometry data were collected using an
627 QExactive hf mass spectrometer coupled to an Easy-nLC-1200™ system. The autosampler
628 typically loads 0.3 µg of reconstituted digest on a 2.5cm C18 trap (New Objective, P/N IT100-
629 25H002) coupled to waste or a 200cm x 75um pillar array column from PharmaFluidics. The
630 column outlet floated at high voltage via a gold connector secured to the micro-cross assembly
631 (IDEX, P/N UH-752). MS1 scans were acquired every 3 sec. with automatic gain control set to

632 3e05 and 60,000 resolution. Ions with 2 to 6 charges were isolated within a 1.2 Th pass window
633 and targeted for HCD activation. The AGC target for HCD was 4E05, 30% NCE, using 75 ms
634 maximum fill time. and 30k resolution at 400 m/z. Searches were performed with both
635 MaxQuant, version 1.6.11 and Byonic search engines (Protein Metrics ver. 2.8.2). Search
636 databases were composed of the Uniprot KB for rat (June 11, 2019). Searches were set to accept
637 static ReDi labels and +57 on Cys residues. Variable oxidation was assumed to occur at Met
638 only. Quantification was achieved by comparing the integrated intensity of each MS1 channel in
639 a sequence-matched triplet derived from the multiplexed sample. Scaffold was used to collate
640 fold enrichment of BSA- and oleate/palmitate + glucose-cultured samples compared to non-
641 peroxide-treated samples. Classifiers to assign active engagement in ISG assembly were
642 established by ROC curve analysis as described(Hung et al., 2016). The $\log_2$ fold enrichment in
643 the peroxide-treated (BSA) samples relative to no peroxide was determined and was generally
644 2.3 or more for biotinylated proteins. For proteins with a $\log_2$ fold change of 1.2 or greater
645 enrichment in the BSA (control) cultured samples, the relative fold change to oleate/palmitate +
646 glucose cultured samples was determined. Protein subcellular locations were determined using
647 annotations from the rat and human orthologs in the UniProt database and additional
648 confirmation by literature searches as needed.

649

650 **Metabolic studies**

651 Mitochondrial function was evaluated using Agilent Seahorse XF96 Extracellular Flux Analyzer.
652 832/3 cells were seeded at a density of 40,000 cells/well in XF 96-well microplates. Cells were
653 cultured for 72 h in BSA (control) or OPG media as indicated. Prior to the assay, cells were

654 washed and incubated in serum-free DMEM supplemented with 5mM HEPES, 2 mM L-
655 glutamine and 1 mM Na pyruvate (Life Technologies), pH 7.40 with either 2 mM or 20 mM
656 glucose. Mitochondrial stress tests were initiated then cellular respiration was evaluated by
657 monitoring the oxygen consumption rate (OCR). A basal rate was established, followed by
658 addition of 2.5 μM oligomycin A, 1.25 μM FCCP, and 2 μM rotenone and antimycin, each as
659 sequential injections. Data were normalized following post-experiment cell enumeration.

660

661 **Quantitative RT-PCR**

662 RNA was harvested using a Zymo RNA minikit and cDNA synthesized in an iScript reaction
663 (Bio Rad). Real-time PCRs were performed using the ABI 7700 sequence detection system and
664 software (Applied Biosystems). All primer sequences are available upon request.

665

666 **Statistical Analysis**

667 Data are presented as the mean ± S.E.M. For statistical significance determinations, data were
668 analyzed by the two-tailed unpaired, Student's t test or by ANOVA with post-hoc analysis for
669 multiple group comparisons as indicated (GraphPad Prism). A p-value < 0.05 was considered
670 significant.

671 **Author contributions**

672 K.E.R., C.K.B., S.C.B. M.R.M., W.S.E., and S.B.S conceived and designed studies. K.E.R.,
673 C.K.B., S.C.B. M.R.M., W.S.E., C.J.B., S.E.B. and S.B.S performed the experiments and
674 analyzed the data. C.Y. and M.R.P. performed proteomics studies. K.E.R., S.C.B. and S.B.S.
675 analyzed proteomics data. J.Z. and Y.W. performed TEM. K.E.R. and S.B.S. wrote the
676 manuscript.

677 **Acknowledgements**

678 We would like to thank Dr. Thomas Rutkowski, Erica Gansemer, and Dr. Ling Yang for helpful
679 comments and discussion and McKenzie Becker for expert technical assistance. We would like
680 to acknowledge the use of the University of Iowa Central Microscopy Research Facility,
681 University of Iowa Proteomics Facility, and University of Iowa Radiation and Free Radical
682 Research Core Facility. This work was supported by startup funds provided by the Fraternal
683 Order of Eagles Diabetes Research Center, University of Iowa to S.B.S., Department of Defense
684 CDMRP grant PR190353 to S.B.S., National Institutes of Health grant R35GM130331 to Y.W.,
685 and a National Institutes of Health Predoctoral Training Grant T32GM008629, PI Daniel Eberl
686 to K.E.R. University of Iowa Electron Spin Resonance (ESR) Facility, Holden Comprehensive
687 Cancer Center, is supported by NCI P30 CA086862.

Competing Interests

No competing interests declared.

690 **Abbreviations**

691 Biotin phenol (BP); dithiothreitol (DTT); glucose (Glc); glucose-stimulated insulin secretion
692 (GSIS); infectious units (IFU); oleate/palmitate (OP); oleate/palmitate + Glc (OPG); oxygen
693 consumption rate (OCR); protein disulfide isomerase (PDI); rat insulin promoter (RIP); Type 2
694 diabetes (T2D); untranslated region (UTR)

695 **Data Availability**

696 The datasets generated during and/or analyzed during the current study are available from the
697 corresponding author upon reasonable request. The mass spectrometry proteomics data have
698 been deposited to the ProteomeXchange Consortium via the PRIDE(Perez-Riverol et al., 2019)
699 partner repository with the dataset identifier PXD028606.

700 **Literature Cited**

701 Alarcon C, Boland BB, Uchizono Y, Moore PC, Peterson B, Rajan S, Rhodes OS, Noske AB,
702 Haataja L, Arvan P, Marsh BJ, Austin J, Rhodes CJ. 2016. Pancreatic β-Cell Adaptive
703 Plasticity in Obesity Increases Insulin Production but Adversely Affects Secretory
704 Function. *Diabetes* **65**:438–450. doi:10.2337/db15-0792

705 Arunagiri A, Haataja L, Cunningham CN, Shrestha N, Tsai B, Qi L, Liu M, Arvan P. 2018.
706 Misfolded proinsulin in the endoplasmic reticulum during development of beta cell failure
707 in diabetes. *Ann N Y Acad Sci* **1418**:5–19. doi:10.1111/nyas.13531

708 Arunagiri A, Haataja L, Pottekat A, Pamenan F, Kim S, Zeltser LM, Paton AW, Paton JC, Tsai
709 B, Itkin-Ansari P, Kaufman RJ, Liu M, Arvan P. 2019. Proinsulin misfolding is an early
710 event in the progression to type 2 diabetes. *Elife* **8**:e44532. doi:10.7554/eLife.44532

711 Bauchle CJ, Rohli KE, Boyer CK, Pal V, Rocheleau JV, Liu S, Imai Y, Taylor EB, Stephens SB.
712 2021. Mitochondrial Efflux of Citrate and Isocitrate Is Fully Dispensable for Glucose-
713 Stimulated Insulin Secretion and Pancreatic Islet β-Cell Function. *Diabetes* db210037.
714 doi:10.2337/db21-0037

715 Bearrows SC, Bauchle CJ, Becker M, Haldeman JM, Swaminathan S, Stephens SB. 2019.
716 Chromogranin B regulates early stage insulin granule trafficking from the Golgi in
717 pancreatic islet beta-cells. *J Cell Sci*. doi:10.1242/jcs.231373

718 Birk J, Meyer M, Aller I, Hansen HG, Odermatt A, Dick TP, Meyer AJ, Appenzeller-Herzog C.
719 2013. Endoplasmic reticulum: reduced and oxidized glutathione revisited. *J Cell Sci*
720 **126**:1604–1617. doi:10.1242/jcs.117218

721 Boersema PJ, Raijmakers R, Lemeer S, Mohammed S, Heck AJ. 2009. Multiplex peptide stable
722 isotope dimethyl labeling for quantitative proteomics. *Nat Protoc* **4**:484–94.
723 doi:10.1038/nprot.2009.21

724 Boland BB, Brown C, Alarcon C, Demozay D, Grimsby JS, Rhodes CJ. 2018. β-Cell Control of
725 Insulin Production During Starvation-Refeeding in Male Rats. *Endocrinology* **159**:895–
726 906. doi:10.1210/en.2017-03120

727 Boland BB, Rhodes CJ, Grimsby JS. 2017. The dynamic plasticity of insulin production in β-
728 cells. *Mol Metab* **6**:958–973. doi:10.1016/j.molmet.2017.04.010

729 Cao M, Mao Z, Kam C, Xiao N, Cao X, Shen C, Cheng KKY, Xu A, Lee K-M, Jiang L, Xia J.
730 2013. PICK1 and ICA69 control insulin granule trafficking and their deficiencies lead to
731 impaired glucose tolerance. *PLoS Biol* **11**:e1001541. doi:10.1371/journal.pbio.1001541

732 Cao X, Lilla S, Cao Z, Pringle MA, Oka OBV, Robinson PJ, Szmaja T, van Lith M, Zanivan S,
733 Bulleid NJ. 2020. The mammalian cytosolic thioredoxin reductase pathway acts via a
734 membrane protein to reduce ER-localised proteins. *J Cell Sci* **133**:jcs241976.
735 doi:10.1242/jcs.241976

736 Delépine M, Nicolino M, Barrett T, Golamaully M, Lathrop GM, Julier C. 2000. EIF2AK3,
737 encoding translation initiation factor 2-alpha kinase 3, is mutated in patients with
738 Wolcott-Rallison syndrome. *Nat Genet* **25**:406–409. doi:10.1038/78085

739 Ellgaard L, Sevier CS, Bulleid NJ. 2018. How Are Proteins Reduced in the Endoplasmic
740 Reticulum? *Trends Biochem Sci* **43**:32–43. doi:10.1016/j.tibs.2017.10.006

741 Engin F, Nguyen T, Yermalovich A, Hotamisligil GS. 2014. Aberrant islet unfolded protein
742 response in type 2 diabetes. *Sci Rep* **4**:4054. doi:10.1038/srep04054

743 Ferdaoussi M, Dai X, Jensen MV, Wang R, Peterson BS, Huang C, Ilkayeva O, Smith N, Miller
744 N, Hajmrle C, Spigelman AF, Wright RC, Plummer G, Suzuki K, Mackay JP, van de Bunt
745 M, Gloyn AL, Ryan TE, Norquay LD, Brosnan MJ, Trimmer JK, Rolph TP, Kibbey RG,
746 Manning Fox JE, Colmers WF, Shirihai OS, Neufer PD, Yeh ETH, Newgard CB,
747 MacDonald PE. 2015. Isocitrate-to-SENP1 signaling amplifies insulin secretion and
748 rescues dysfunctional β cells. *J Clin Invest* **125**:3847–3860. doi:10.1172/JCI82498

749 Gandasi NR, Yin P, Omar-Hmeadi M, Ottosson Laakso E, Vikman P, Barg S. 2018. Glucose-
750 Dependent Granule Docking Limits Insulin Secretion and Is Decreased in Human Type 2
751 Diabetes. *Cell Metab* **27**:470-478 e4. doi:10.1016/j.cmet.2017.12.017

752 Gansemer ER, McCommis KS, Martino M, King-McAlpin AQ, Potthoff MJ, Finck BN, Taylor EB,
753 Rutkowski DT. 2020. NADPH and Glutathione Redox Link TCA Cycle Activity to
754 Endoplasmic Reticulum Homeostasis. *iScience* **23**:101116.
755 doi:10.1016/j.isci.2020.101116

756 Gautier A, Juillerat A, Heinis C, Correa IR, Kindermann M, Beaufils F, Johnsson K. 2008. An
757 engineered protein tag for multiprotein labeling in living cells. *Chem Biol* **15**:128–36.
758 doi:10.1016/j.chembiol.2008.01.007

759 Gembal M, Gilon P, Henquin JC. 1992. Evidence that glucose can control insulin release
760 independently from its action on ATP-sensitive K+ channels in mouse B cells. *J Clin*
761 *Invest* **89**:1288–1295. doi:10.1172/JCI115714

762 Ghiasi SM, Dahlby T, Hede Andersen C, Haataja L, Petersen S, Omar-Hmeadi M, Yang M, Pihl
763 C, Bresson SE, Khilji MS, Klindt K, Cheta O, Perone MJ, Tyrberg B, Prats C, Barg S,
764 Tengholm A, Arvan P, Mandrup-Poulsen T, Marzec MT. 2019. Endoplasmic Reticulum
765 Chaperone Glucose-Regulated Protein 94 Is Essential for Proinsulin Handling. *Diabetes*
766 **68**:747–760. doi:10.2337/db18-0671

767 Guest PC, Rhodes CJ, Hutton JC. 1989. Regulation of the biosynthesis of insulin-secretory-
768 granule proteins. Co-ordinate translational control is exerted on some, but not all,
769 granule matrix constituents. *Biochem J* **257**:431–7.

770 Haataja L, Arunagiri A, Hassan A, Regan K, Tsai B, Dhayalan B, Weiss MA, Liu M, Arvan P.
771 2021. Distinct states of proinsulin misfolding in MIDY. *Cell Mol Life Sci* **78**:6017–6031.
772 doi:10.1007/s00018-021-03871-1

773 Halban PA, Polonsky KS, Bowden DW, Hawkins MA, Ling C, Mather KJ, Powers AC, Rhodes
774 CJ, Sussel L, Weir GC. 2014. beta-cell failure in type 2 diabetes: postulated
775 mechanisms and prospects for prevention and treatment. *Diabetes Care* **37**:1751–8.
776 doi:10.2337/dc14-0396

777 Han J, Song B, Kim J, Kodali VK, Pottekat A, Wang M, Hassler J, Wang S, Pennathur S, Back
778 SH, Katze MG, Kaufman RJ. 2015. Antioxidants Complement the Requirement for

779 Protein Chaperone Function to Maintain β-Cell Function and Glucose Homeostasis.
780 *Diabetes* **64**:2892–2904. doi:10.2337/db14-1357

781 Harding HP, Zeng H, Zhang Y, Jungries R, Chung P, Plesken H, Sabatini DD, Ron D. 2001.
782 Diabetes mellitus and exocrine pancreatic dysfunction in perk-/- mice reveals a role for
783 translational control in secretory cell survival. *Mol Cell* **7**:1153–1163. doi:10.1016/s1097-
784 2765(01)00264-7

785 Hassler JR, Scheuner DL, Wang S, Han J, Kodali VK, Li P, Nguyen J, George JS, Davis C, Wu
786 SP, Bai Y, Sartor M, Cavalcoli J, Malhi H, Baudouin G, Zhang Y, Yates JR, Itkin-Ansari
787 P, Volkmann N, Kaufman RJ. 2015. The IRE1α/XBP1s Pathway Is Essential for the
788 Glucose Response and Protection of β Cells. *PLoS Biol* **13**:e1002277.
789 doi:10.1371/journal.pbio.1002277

790 Hayes HL, Peterson BS, Haldeman JM, Newgard CB, Hohmeier HE, Stephens SB. 2017.
791 Delayed apoptosis allows islet beta-cells to implement an autophagic mechanism to
792 promote cell survival. *PLoS One* **12**:e0172567. doi:10.1371/journal.pone.0172567

793 Haythorne E, Rohm M, van de Bunt M, Brereton MF, Tarasov AI, Blacker TS, Sachse G, Silva
794 Dos Santos M, Terron Exposito R, Davis S, Baba O, Fischer R, Duchen MR, Rorsman
795 P, MacRae JI, Ashcroft FM. 2019. Diabetes causes marked inhibition of mitochondrial
796 metabolism in pancreatic β-cells. *Nat Commun* **10**:2474. doi:10.1038/s41467-019-
797 10189-x

798 Henquin JC. 2009. Regulation of insulin secretion: a matter of phase control and amplitude
799 modulation. *Diabetologia* **52**:739–751. doi:10.1007/s00125-009-1314-y

800 Henquin JC, Ishiyama N, Nenquin M, Ravier MA, Jonas JC. 2002. Signals and pools underlying
801 biphasic insulin secretion. *Diabetes* **51 Suppl 1**:S60-7.

802 Hohmeier HE, Mulder H, Chen G, Henkel-Rieger R, Prentki M, Newgard CB. 2000. Isolation of
803 INS-1-derived cell lines with robust ATP-sensitive K+ channel-dependent and -
804 independent glucose-stimulated insulin secretion. *Diabetes* **49**:424–30.

805 Hsu J-L, Huang S-Y, Chow N-H, Chen S-H. 2003. Stable-isotope dimethyl labeling for
806 quantitative proteomics. *Anal Chem* **75**:6843–6852. doi:10.1021/ac0348625

807 Hung V, Udeshi ND, Lam SS, Loh KH, Cox KJ, Pedram K, Carr SA, Ting AY. 2016. Spatially
808 resolved proteomic mapping in living cells with the engineered peroxidase APEX2. *Nat*
809 *Protoc* **11**:456–75. doi:10.1038/nprot.2016.018

810 Ivarsson R, Quintens R, Dejonghe S, Tsukamoto K, in ’t Veld P, Renstrom E, Schuit FC. 2005.
811 Redox control of exocytosis: regulatory role of NADPH, thioredoxin, and glutaredoxin.
812 *Diabetes* **54**:2132–42.

813 Jang I, Pottekat A, Poothong J, Yong J, Lagunas-Acosta J, Charbono A, Chen Z, Scheuner DL,
814 Liu M, Itkin-Ansari P, Arvan P, Kaufman RJ. 2019. PDIA1/P4HB is required for efficient
815 proinsulin maturation and ß cell health in response to diet induced obesity. *Elife*
816 **8**:e44528. doi:10.7554/eLife.44528

817 Joshi G, Chi Y, Huang Z, Wang Y. 2014. Aβ-induced Golgi fragmentation in Alzheimer's disease
818 enhances Aβ production. *Proc Natl Acad Sci U S A* **111**:E1230-1239.
819 doi:10.1073/pnas.1320192111

820 Kahn SE, Halban PA. 1997. Release of incompletely processed proinsulin is the cause of the
821 disproportionate proinsulinemia of NIDDM. *Diabetes* **46**:1725–32.

822 Kahn SE, Zraika S, Utzschneider KM, Hull RL. 2009. The beta cell lesion in type 2 diabetes:
823 there has to be a primary functional abnormality. *Diabetologia* **52**:1003–12.
824 doi:10.1007/s00125-009-1321-z

825 Kang T, Boland BB, Alarcon C, Grimsby JS, Rhodes CJ, Larsen MR. 2019. Proteomic Analysis
826 of Restored Insulin Production and Trafficking in Obese Diabetic Mouse Pancreatic
827 Islets Following Euglycemia. *J Proteome Res* **18**:3245–3258.
828 doi:10.1021/acs.jproteome.9b00160

829 Kim D-S, Song L, Wang J, Wu H, Gu G, Sugi Y, Li Z, Wang H. 2018. GRP94 Is an Essential
830 Regulator of Pancreatic β-Cell Development, Mass, and Function in Male Mice.
831 *Endocrinology* **159**:1062–1073. doi:10.1210/en.2017-00685

832 Lam SS, Martell JD, Kamer KJ, Deerinck TJ, Ellisman MH, Mootha VK, Ting AY. 2015. Directed
833 evolution of APEX2 for electron microscopy and proximity labeling. *Nat Methods* **12**:51–
834 4. doi:10.1038/nmeth.3179

835 Like AA, Chick WL. 1970. Studies in the diabetic mutant mouse. II. Electron microscopy of
836 pancreatic islets. *Diabetologia* **6**:216–242. doi:10.1007/BF01212232

837 Lipson KL, Fonseca SG, Ishigaki S, Nguyen LX, Foss E, Bortell R, Rossini AA, Urano F. 2006.
838 Regulation of insulin biosynthesis in pancreatic beta cells by an endoplasmic reticulum-
839 resident protein kinase IRE1. *Cell Metab* **4**:245–254. doi:10.1016/j.cmet.2006.07.007

840 Liu M, Hodish I, Rhodes CJ, Arvan P. 2007. Proinsulin maturation, misfolding, and
841 proteotoxicity. *Proc Natl Acad Sci U S A* **104**:15841–6. doi:10.1073/pnas.0702697104

842 Malhotra JD, Miao H, Zhang K, Wolfson A, Pennathur S, Pipe SW, Kaufman RJ. 2008.
843 Antioxidants reduce endoplasmic reticulum stress and improve protein secretion. *Proc*
844 *Natl Acad Sci U S A* **105**:18525–18530. doi:10.1073/pnas.0809677105

845 Marchetti P, Bugliani M, Lupi R, Marselli L, Masini M, Boggi U, Filipponi F, Weir GC, Eizirik DL,
846 Cnop M. 2007. The endoplasmic reticulum in pancreatic beta cells of type 2 diabetes
847 patients. *Diabetologia* **50**:2486–2494. doi:10.1007/s00125-007-0816-8

848 Masini M, Marselli L, Bugliani M, Martino L, Masiello P, Marchetti P, De Tata V. 2012.
849 Ultrastructural morphometric analysis of insulin secretory granules in human type 2
850 diabetes. *Acta Diabetol* **49 Suppl 1**:S247-252. doi:10.1007/s00592-012-0446-6

851 Muller A, Neukam M, Ivanova A, Sonmez A, Munster C, Kretschmar S, Kalaidzidis Y, Kurth T,
852 Verbavatz JM, Solimena M. 2017. A Global Approach for Quantitative Super Resolution
853 and Electron Microscopy on Cryo and Epoxy Sections Using Self-labeling Protein Tags.
854 *Sci Rep* **7**:23. doi:10.1038/s41598-017-00033-x

855 Ozcan U, Yilmaz E, Ozcan L, Furuhashi M, Vaillancourt E, Smith RO, Görgün CZ, Hotamisligil
856 GS. 2006. Chemical chaperones reduce ER stress and restore glucose homeostasis in a
857 mouse model of type 2 diabetes. *Science* **313**:1137–1140. doi:10.1126/science.1128294

858 Pasquier A, Vivot K, Erbs E, Spiegelhalter C, Zhang Z, Aubert V, Liu Z, Senkara M, Maillard E,
859 Pinget M, Kerr-Conte J, Pattou F, Marciniak G, Ganzhorn A, Ronchi P, Schieber NL,
860 Schwab Y, Saftig P, Goginashvili A, Ricci R. 2019. Lysosomal degradation of newly
861 formed insulin granules contributes to β cell failure in diabetes. *Nat Commun* **10**:3312.
862 doi:10.1038/s41467-019-11170-4

863 Perez-Riverol Y, Csordas A, Bai J, Bernal-Llinares M, Hewapathirana S, Kundu DJ, Inuganti A,
864 Griss J, Mayer G, Eisenacher M, Pérez E, Uszkoreit J, Pfeuffer J, Sachsenberg T,
865 Yilmaz S, Tiwary S, Cox J, Audain E, Walzer M, Jarnuczak AF, Ternent T, Brazma A,
866 Vizcaíno JA. 2019. The PRIDE database and related tools and resources in 2019:
867 improving support for quantification data. *Nucleic Acids Res* **47**:D442–D450.
868 doi:10.1093/nar/gky1106

869 Reinbothe TM, Ivarsson R, Li D-Q, Niazi O, Jing X, Zhang E, Stenson L, Bryborn U, Renström
870 E. 2009. Glutaredoxin-1 Mediates NADPH-Dependent Stimulation of Calcium-
871 Dependent Insulin Secretion. *Molecular Endocrinology* **23**:893–900.
872 doi:10.1210/me.2008-0306

873 Reissaus CA, Piñeros AR, Twigg AN, Orr KS, Conteh AM, Martinez MM, Kamocka MM, Day
874 RN, Tersey SA, Mirmira RG, Dunn KW, Linnemann AK. 2019. A Versatile, Portable
875 Intravital Microscopy Platform for Studying Beta-cell Biology In Vivo. *Sci Rep* **9**:8449.
876 doi:10.1038/s41598-019-44777-0

877 Rhodes CJ, Alarcon C. 1994. What beta-cell defect could lead to hyperproinsulinemia in
878 NIDDM? Some clues from recent advances made in understanding the proinsulin-
879 processing mechanism. *Diabetes* **43**:511–7.

880 Ronnebaum SM, Ilkayeva O, Burgess SC, Joseph JW, Lu D, Stevens RD, Becker TC, Sherry
881 AD, Newgard CB, Jensen MV. 2006. A pyruvate cycling pathway involving cytosolic
882 NADP-dependent isocitrate dehydrogenase regulates glucose-stimulated insulin
883 secretion. *J Biol Chem* **281**:30593–602. doi:M511908200 [pii] 10.1074/jbc.M511908200

884 Sharma RB, O'Donnell AC, Stamateris RE, Ha B, McCloskey KM, Reynolds PR, Arvan P,
885 Alonso LC. 2015. Insulin demand regulates β cell number via the unfolded protein
886 response. *J Clin Invest* **125**:3831–3846. doi:10.1172/JCI79264

887 Shrestha N, Liu T, Ji Y, Reinert RB, Torres M, Li X, Zhang M, Tang C-HA, Hu C-CA, Liu C, Naji
888 A, Liu M, Lin JD, Kersten S, Arvan P, Qi L. 2020. Sel1L-Hrd1 ER-associated degradation
889 maintains β cell identity via TGF-β signaling. *J Clin Invest* **130**:3499–3510.
890 doi:10.1172/JCI134874

891 Stephens SB, Edwards RJ, Sadahiro M, Lin WJ, Jiang C, Salton SR, Newgard CB. 2017. The
892 Prohormone VGF Regulates beta Cell Function via Insulin Secretory Granule
893 Biogenesis. *Cell Rep* **20**:2480–2489. doi:10.1016/j.celrep.2017.08.050

894 Støy J, Steiner DF, Park S-Y, Ye H, Philipson LH, Bell GI. 2010. Clinical and molecular genetics
895 of neonatal diabetes due to mutations in the insulin gene. *Rev Endocr Metab Disord*
896 **11**:205–215. doi:10.1007/s11154-010-9151-3

897 Tran DT, Pottekat A, Mir SA, Loguercio S, Jang I, Campos AR, Scully KM, Lahmy R, Liu M,
898 Arvan P, Balch WE, Kaufman RJ, Itkin-Ansari P. 2020. Unbiased Profiling of the Human
899 Proinsulin Biosynthetic Interaction Network Reveals a Role for Peroxiredoxin 4 in
900 Proinsulin Folding. *Diabetes* **69**:1723–1734. doi:10.2337/db20-0245

901 Uchizono Y, Alarcón C, Wicksteed BL, Marsh BJ, Rhodes CJ. 2007. The balance between
902 proinsulin biosynthesis and insulin secretion: where can imbalance lead? *Diabetes Obes*
903 *Metab* **9 Suppl 2**:56–66. doi:10.1111/j.1463-1326.2007.00774.x

904 Ward WK, Bolgiano DC, McKnight B, Halter JB, Porte D. 1984. Diminished B cell secretory
905 capacity in patients with noninsulin-dependent diabetes mellitus. *J Clin Invest* **74**:1318–
906 28. doi:10.1172/JCI111542

907 Wicksteed B, Alarcon C, Briaud I, Lingohr MK, Rhodes CJ. 2003. Glucose-induced translational
908 control of proinsulin biosynthesis is proportional to preproinsulin mRNA levels in islet
909 beta-cells but not regulated via a positive feedback of secreted insulin. *J Biol Chem*
910 **278**:42080–42090. doi:10.1074/jbc.M303509200

911 Winter J, Klappa P, Freedman RB, Lilie H, Rudolph R. 2002. Catalytic activity and chaperone
912 function of human protein-disulfide isomerase are required for the efficient refolding of
913 proinsulin. *J Biol Chem* **277**:310–317. doi:10.1074/jbc.M107832200

914 Xin Y, Dominguez Gutierrez G, Okamoto H, Kim J, Lee A-H, Adler C, Ni M, Yancopoulos GD,
915 Murphy AJ, Gromada J. 2018. Pseudotime Ordering of Single Human β-Cells Reveals
916 States of Insulin Production and Unfolded Protein Response. *Diabetes* **67**:1783–1794.
917 doi:10.2337/db18-0365

918 Xu T, Yang L, Yan C, Wang Xiaoxia, Huang P, Zhao F, Zhao L, Zhang M, Jia W, Wang
919 Xiangdong, Liu Y. 2014. The IRE1α-XBP1 pathway regulates metabolic stress-induced
920 compensatory proliferation of pancreatic β-cells. *Cell Res* **24**:1137–1140.
921 doi:10.1038/cr.2014.55

922 Yong J, Johnson JD, Arvan P, Han J, Kaufman RJ. 2021. Therapeutic opportunities for
923 pancreatic β-cell ER stress in diabetes mellitus. *Nat Rev Endocrinol* **17**:455–467.
924 doi:10.1038/s41574-021-00510-4

925 Yu CL, Brooks S, Li Y, Subramanian M, Summers R, Pope M. 2017. Rapid Proteomics to
926 Prospect and Validate Novel Bacterial Metabolism Induced by Environmental Burden.
927 *Methods Enzymol* **586**:379–411. doi:10.1016/bs.mie.2016.11.003

928 Zougman A, Selby PJ, Banks RE. 2014. Suspension trapping (STrap) sample preparation
929 method for bottom-up proteomics analysis. *Proteomics* **14**:1006–1000.
930 doi:10.1002/pmic.201300553

931

932

933 **Figure legends**

934 **Figure 1. Insulin granule formation is impaired in a rodent model of islet dysfunction.** 8-10
935 week old male C57BL6/J mice (n=5-9) were placed on a standard chow (SC) or Western diet
936 (WD). Body weight (**A**) and *ad lib* fed blood glucose (**B**) were recorded weekly. After 8 wk of
937 diet, 4 h fasted mice were injected i.p. with 1 mg/g bw glucose and blood glucose monitored for
938 2 h as indicated (**C**) and plasma sampled for insulin (**D**). (**E**) Model of the proCpepSNAP
939 reporter with SNAPtag inserted within the C-peptide region of human preproinsulin. (**F**)
940 Schematic of proCpepSNAP pulse-chase labeling timeline. (**G-I**) Mouse islets (8 wk, SC vs.
941 WD C57BL6/J) were treated with AdRIP-proCpepSNAP. 48 h post-infection, islets were pulse-
942 labeled with SNAP-505 for 20 min (green), chased for 2 h, immunostained for GM130
943 (magenta), and counterstained with DAPI (blue). Confocal images were collected (**G**), and the
944 total number of proCpepSNAP-labeled nascent granules quantified (**H**) (n=4; 22-25 cells per
945 mouse). (**I**) Frequency distribution of binned proCpepSNAP-labeled granule distances (microns)
946 from the Golgi were quantified (n=4). proCpepSNAP pulse-chase labeling of β-cells from
947 C57BL6/J mice (14 wk, SC or WD, n=5) were imaged by TIRF microscopy (**J**) and the total
948 number of plasma membrane (PM)-bound proCpepSNAP-labeled granules are quantified (**K**)
949 (n=5-7; 26-57 cells per mouse). (**G**, **J**) Scale bar = 5 μm. (**A-D**, **H**, **I**, **K**) Data represent the
950 mean ± S.E.M. * $p < 0.05$ by two-way ANOVA with Sidak post-test analysis (**A-D**, **I**) or Student
951 t test (**H**, **K**).

952

953 **Figure 2. Elevated glucose and fatty acid culture impair β-cell function and proinsulin**
954 **trafficking.** (**A-B**) 10-14 week old C57BLKS/J db/+ and db/db mice (n=4-5 per group) were

955 fasted for 4 h and injected i.p. with 1mg/g bw glucose. Blood glucose was monitored for 2 h as
956 indicated (**A**) and plasma was sampled for insulin (**B**). Islet lysates from 10-14 wk old
957 C57BLKS/J db/+ vs. db/db mice were analyzed by immunoblots (**C**) and relative protein
958 expression quantified following normalization to the tubulin loading control (**D**). (**E**-**N**) 832/3
959 cells were cultured for 72 h in control media supplemented with BSA, media containing
960 oleate:palmitate (2:1, 1mM OP), or media containing oleate/palmitate (2:1, 1 mM) and elevated
961 glucose (20mM; OPG) as indicated. (**E**) Glucose-stimulated insulin secretion was measured by
962 static incubation in media containing 2.5 mM Glc followed by 12 mM Glc for 1 h each.
963 Immunoblots from whole-cell lysates were probed with CgB, PC2, and CPE antibodies are
964 shown (**F**) and relative protein expression was quantified following normalization to the tubulin
965 loading control (**G**) (n=3). 832/3 cells stably expressing proCpepSNAP were pulse-labeled with
966 SNAP-505 for 20 min (green), chased for 2 h (**H**, **I**), 4 h (**J**, **K**), or 18-20 h (**L**, **M**),
967 immunostained for TGN38 (magenta) and counterstained with DAPI (blue). Representative
968 images of 2 h chase are shown (**H**) and frequency distribution of binned proCpepSNAP-labeled
969 nascent granule distance from the Golgi determined (**I**) (n=6; 35-37 cells per group; scale bar = 5
970 μm). The total number of nascent (proCpepSNAP-labeled) insulin granules bound to the plasma
971 membrane (PM) via TIRF microscopy after a 4 h chase is shown (**J**) and normalized to cell area
972 (**K**) (n=3; 4 images per condition). The total number of nascent (proCpepSNAP-labeled) insulin
973 granules following a 18 h chase is shown (**L**) and quantified (**M**) (61-63 cells per condition,
974 n=3). (**N**) Cell lysates were resolved on 8-23% iodixanol density gradients. Solid line represents
975 insulin as determined by ELISA from gradient fractions; dotted line represents gradient density
976 (absorbance at 340 nm). (**A**, **B**, **D**, **E**, **G**, **I**, **K**, **M**) Data represent the mean ± S.E.M. * $p < 0.05$
977 by repeated measures ANOVA with Sidak post-test analysis (**A**, **B**), Student t test (**D**, **K**, **M**), or

978 two-way ANOVA with Sidak post-test analysis (**E**, **G**, **I**). (**E**) * comparison of secretion response
979 at stimulatory glucose to control (BSA, 7.5 mM); # comparison of secretion response at basal
980 glucose to control (BSA, 7.5 mM).

981

982 **Figure 3. APEX2 labeling reveals increased proinsulin interactions with ER resident**
983 **proteins in 832/3 cells cultured with elevated glucose and fatty acids.** (**A**) 832/3 cells
984 expressing proCpepAPEX2 were immunostained for insulin (green), V5 (proCpepV5APEX2,
985 red), TGN38 (magenta), and counterstained with DAPI (blue). Scale bar = 5 μm. (**B**)
986 proCpepAPEX2 expressing 832/3 cells were treated with biotin-phenol (BP) and H_2O_2 as
987 indicated. Cell lysates were analyzed by Western blot probed with fluorescent streptavidin or
988 proinsulin antibody. (**C**) Aliquots of whole cell lysates compared to Neutravidin (NA) agarose
989 resin-enriched fractions were resolved by LDS-NuPAGE and analyzed by Coomassie blue
990 staining. (**D**, **E**) Neutravidin agarose purified proteins from proCpepAPEX2 expressing 832/3
991 cells treated with or without H_2O_2 were identified by quantitative proteomics (n=4). Proteins
992 enriched 1.2-fold or greater in peroxide-treated compared to non-peroxide-treated samples are
993 displayed by mean-$\log_2$-fold enrichment as a function of subcellular location (**D**) or as a heatmap
994 to visualize the changes of individual proteins (**E**). (**F-H**) 832/3 cells stably expressing
995 proCpepAPEX2 were cultured for 72 h in control media supplemented with BSA or media
996 containing oleate/palmitate (2:1, 1 mM) and elevated glucose (20 mM; OPG) as indicated. Cell
997 lysates were analyzed by Western blot probed with fluorescent streptavidin (**F**). (**G, H**)
998 Neutravidin agarose purified proteins were identified by quantitative proteomics. Proteins
999 enriched 1.2-fold or greater in BSA (control) cultured cells compared to non-peroxide treated
1000 samples were further analyzed as the mean (n=4) of the relative fold ($\log_2$) change of OPG

1001 compared to BSA cultured cells. Data are displayed as a function of subcellular location for
1002 individual proteins (**G**) and as a heatmap (**H**).

1003

1004 **Figure 4. Delayed ER export of proinsulin in animal and cell culture models of**
1005 **hyperglycemia.** (**A-E**) 832/3 cells were cultured for up to 72 h in control media supplemented
1006 with BSA or media containing oleate/palmitate (2:1, 1 mM) and elevated glucose (20 mM; OPG)
1007 as indicated. Cell lysates were analyzed by immunoblot (**A**) and quantified following
1008 normalization to the tubulin loading control (**B**) (n=3). (**C**) mRNA expression levels were
1009 determined by qRT-PCR (n=3). (**D-E**) 832/3 cells stably expressing proCpepSNAP were pulse-
1010 labeled with SNAP-505 for 20 min (green) then fixed and immunostained for GRP94 (red),
1011 TGN38 (magenta), and counterstained with DAPI (blue). Representative images (**D**) are shown
1012 (scale bar = 5 μm) and the ratio of proCpepSNAP fluorescence coincident with the Golgi
1013 compared to ER quantified (**E**) (n=6-8; 48-64 cells). (**F-G**) Isolated mouse islets (C57BLKS/J
1014 db/+ vs. db/db) were treated with AdRIP-proCpepSNAP. 48 h post-infection, islets were pulse-
1015 labeled with SNAP-505 for 20 min (green), chased for 10 min, immunostained for GM130
1016 (magenta), and counterstained with DAPI (blue). Representative images (**F**) are shown (scale
1017 bar = 3 μm) and the ratio of proCpepSNAP fluorescence coincident with the Golgi compared to
1018 ER quantified (**G**) (n=4; 6-36 cells). (**B**, **C**, **E**, **G**) Data represent the mean ± S.E.M. * $p < 0.05$
1019 by Student t test (**B**, **C**, **E**, **G**).

1020

1021 **Figure 5. Delayed ER export delay of proinsulin is specific and independent of overt ER**
1022 **stress.** (**A**) Islets isolated from C57BLKS/J db/+ vs. db/db (n=3) were examined for

1023 ultrastructure by electron microscopy and representative micrographs depicting the ER are
1024 shown. (**B**, **E-G**) 832/3 cells were cultured for 72 h in control media supplemented with BSA,
1025 media containing oleate:palmitate (2:1, 1 mM OP) or media containing oleate:palmitate (2:1, 1
1026 mM) and elevated glucose (20 mM; OPG) as indicated. (**B**) mRNA expression was examined by
1027 qRT-PCR (n=4-6). Cells were treated for 18 h with thapsigargin (50 nM) as indicated. (**C**)
1028 832/3 cells treated with AdRIP-CgB-CLIP were analyzed by immunoblot with antibodies raised
1029 against CLIP or endogenous CgB as indicated. (**D**) 832/3 cells expressing proCpepSNAP and
1030 CgB-CLIP were pulse-labeled with SNAP-505 (green) and CLIP-TMR (red) for 20 min, chased
1031 for 2 h, prior to fixation. Cells were immunostained for TGN38 (magenta), and counterstained
1032 with DAPI (blue). Representative images are shown (scale bar = 5 μm). (**E-G**) 832/3 cells
1033 expressing proCpepSNAP and CgB-CLIP were pulse-labeled with SNAP-505 (green) and CLIP-
1034 TMR (red) for 20 min, fixed and immunostained for TGN38 (magenta), and counterstained with
1035 DAPI (blue). (**E**) Representative images are shown (scale bar = 5 μm). Mander's correlation
1036 coefficient (MCC) was used to determine colocalization of labeled proCpepSNAP (SNAP) vs
1037 CgB-CLIP (CLIP) with TGN38 (**F**) or proCpepSNAP (SNAP) with CgB-CLIP (CLIP) as
1038 indicated (**G**) (n=3; 53-70 cells per condition). (**B**, **F**, **G**) Data represent the mean ± S.E.M. * $p <$
1039 0.05 by two-way ANOVA with Sidak post-test analysis (**B**, **F**) or Student t test (**G**).

1040

1041 **Figure 6. Proinsulin ER export delay can be rescued by chemical reducing agent.** 832/3
1042 cells were cultured for 72 h in control media supplemented with BSA (1%) or media containing
1043 oleate/palmitate (2:1, 1 mM) and elevated glucose (20 mM; OPG) as indicated. (**A**) Oxygen
1044 consumption rate (OCR) was measured at stimulatory glucose (20 mM) and following sequential
1045 addition of oligomycin (2.5 μM), FCCP (1.25 μM), and rotenone plus antimycin A (2 μM) as

1046 indicated (n=3 independent experiments). (**B**) 832/3 cells treated with AdRIP-Grx1-roGFP2
1047 were imaged at 470/535 nm and 395/510 nm and re-imaged following DTT (10 mM) and
1048 diamide (5 mM) treatment for 12 minutes each (n=5). Ratiometric intensities were normalized to
1049 DTT (0%) and diamide (100%). (**C**) Cell ROX staining was used to measure ROS with 1 h
1050 menadione treatment (Men; 100 μM) as a positive control (n=3). (**D, E**) 832/3 cells stably
1051 expressing proCpepSNAP were treated with vehicle (control) or DTT (0.5 mM) for 4 h prior to
1052 being pulse-labeled with SNAP-505 for 20 min (green), fixed, and immunostained for TGN38
1053 (magenta), and counterstained with DAPI (blue). Representative images (**D**) are shown (scale
1054 bar = 5 μm) and Mander's correlation coefficient (**E**) was used to determine the colocalization of
1055 labeled proCpepSNAP (SNAP) with TGN38 (n=3-4; 71-91 cells per condition). (**F**) Model
1056 depicting metabolic regulation of ER redox homeostasis and proinsulin export via NADPH
1057 production and glutathione reduction created by Biorender. (**A-C**, **E**) Data represent the mean ±
1058 S.E.M. * $p < 0.05$ by two-way ANOVA with Sidak post-test analysis (**A**, **E**), one-way ANOVA
1059 with Dunnet post-test analysis (**C**), or Student t test (**B**).

1060

1061 **Figure 7. Loss of cytosolic NADPH-producing enzyme Idh1 impairs insulin granule**
1062 **formation.** (**A**) Model depicting metabolic regulation of ER redox homeostasis and proinsulin
1063 export via NADPH production and glutathione reduction created by Biorender. **(B-F**) Mouse
1064 islets were co-treated with AdRIP-proCpepSNAP and either Ad-shRNA-SAFE (control) or Ad-
1065 shRNA-Idh1 and analyzed after 72 h. (**B**) Idh1 mRNA expression was determined by qRT-PCR
1066 (n=4-5). (**C-F**) Mouse islets were pulse-labeled with SNAP-505 for 20 min (green) and chased
1067 for 2 h. Cells were fixed, immunostained for GM130 (magenta), and counterstained with DAPI
1068 (blue). mCherry expression was used to identify shRNA-expressing cells in each condition.

1069 Total number of nascent (proCpepSNAP-labeled) granules per mCherry+ cell was quantified (**C**)
1070 (n=4; 4-11 cells per mouse) and representative images shown (**D**) (scale bar = 2 μm). (**E, F**)
1071 Mouse islets were treated with vehicle (control) or DTT (0.5 mM) for 4 h prior to being pulse-
1072 labeled. Representative images (**E**) are shown from pulse-chase labeling and quantified per
1073 mCherry+ cell (**F**) (n=3-5; 32-54 cells per condition). (**B, C, F**) Data represent the mean ±
1074 S.E.M. * $p < 0.05$ by Student t test (**B**, **C**) or two-way ANOVA with Sidak post-test analysis (**F**).

1075

1076 **Figure 8. Model of metabolism-coupled proinsulin trafficking.** In this model, glucose
1077 metabolism by the mitochondria generates NADPH, which is used to regulate glutathione
1078 cycling (GSH/GSSG) and produce GSH reducing equivalents. GSH is necessary to maintain
1079 sequential rounds of protein disulfide bond isomerization (R-SH, R-SS-R) in the ER to facilitate
1080 proinsulin folding. Properly folded proinsulin can be exported from the ER to the Golgi, where
1081 it is packaged into immature secretory granules. In response to nutrient excess in T2D,
1082 mitochondrial dysfunction leads to a decrease in NADPH and an insufficient supply of GSH
1083 reducing equivalents to sustain proinsulin folding. This leads to a delay in proinsulin ER export
1084 and ultimately a reduction in the production of insulin secretory granules. Proinsulin NMR
1085 structure (2KQP) was derived from the RCSB protein database. This model was created with
1086 Biorender.com.

1087

1088 **Supplemental figure legends**

1089 **Figure S1. Schematic of proCpepSNAP pulse-chase labeling**. To examine proinsulin
1090 trafficking, islet cells or 832/3 cells expressing proCpepSNAP are initially treated with
1091 SNAPcell block to non-fluorescently label pre-existing proCpepSNAP. Following culture to
1092 allow for *de novo* proCpepSNAP synthesis, cells are fluorescently labeled with SNAPcell-505
1093 (green), and then chased in culture media as indicated prior to fixation to examine ER-Golgi
1094 transit and post-Golgi insulin granule formation. An analogous labeling scheme is performed for
1095 CgB-CLIP. This model was created in Biorender.

1096

1097 **Figure S2. Affinity purification of APEX2 labeling in 832/3 cells**. 832/3 cells expressing
1098 proCpepAPEX2 were treated with H_2O_2 as indicated. (**A**) Lysates from proCpepAPEX2-
1099 biotinylated cells were enriched using Neutravidin agarose resin and various stages of
1100 purification analyzed by immunoblot probed with GRP94, CgB, and Syntaxin-4 antibodies. (**B**)
1101 832/3 cells expressing proCpepAPEX2 were cultured for 72 h in control media supplemented
1102 with BSA or media containing oleate/palmitate (2:1, 1 mM) and elevated glucose (20 mM; OPG)
1103 as indicated. Neutravidin agarose-enriched lysates compared to whole cell lysates were analyzed
1104 by immunoblot as indicated.

1105

1106 **Figure S3. ER export delay of proinsulin is independent of ER stress in OPG-cultured**
1107 **832/3 cells.** 832/3 cells were cultured for 72 h in control media supplemented with BSA, media
1108 containing oleate:palmitate (2:1, 1 mM OP) or media containing oleate:palmitate (2:1, 1 mM)
1109 and elevated glucose (20 mM; OPG) as indicated. Cell lysates were analyzed by immunoblot

1110 compared to cells treated for 18 h with thapsigargin (50 nM) as indicated. (**B**) 832/3 cells stably
1111 expressing proCpepSNAP were pretreated with TUDCA (10 μM) or vehicle control (DMSO) for
1112 4 h, as indicated, prior to being pulse-labeled with SNAP-505 for 20 min (green), fixed, and
1113 counterstained with DAPI (blue). Representative images are shown (scale bar = 5 μm).

1114

1115 **Figure S4. DTT treatment restores ER proinsulin export delay in OPG-cultured 832/3 cells.**
1116 (**A**-**C**, **F**) 832/3 cells were cultured for 72 h in control media supplemented with BSA (1%) or
1117 media containing oleate/palmitate (2:1, 1 mM) and elevated glucose (20 mM; OPG) as indicated.
1118 (**A**-**C**) Oxygen consumption rate was measured at stimulatory glucose (20 mM) and following
1119 sequential addition of oligomycin (2.5 μM), FCCP (1.25 μM), and rotenone plus antimycin A (2
1120 μM). Basal respiration (**A**), maximum respiration (**B**), and ATP production (**C**) were calculated
1121 (n=3, up to 15 replicates per condition). (**D**) Isolated islets (n=4 mice) were cultured overnight
1122 with vehicle or DTT (0.5 mM). Glucose-stimulated insulin secretion was measured by static
1123 incubation in media containing 2.5 mM Glc followed by 12 mM Glc for 1 h each. (**E**) 832/3
1124 cells expressing Grx1-roGFP2 were treated with the indicated concentrations of DTT for 12 min
1125 and imaged at 470/535 nm and 395/510 nm. Ratiometric intensities were normalized to cells
1126 treated with DTT (1mM; 0%) and diamide (5 μM; 100%). (**F**) 832/3 cells stably expressing
1127 proCpepSNAP were treated with DTT (0.5 mM) for 4 h prior to being pulse-labeled with SNAP-
1128 505 for 20 min (green), fixed, and immunostained for TGN38 (magenta), and counterstained
1129 with DAPI (blue). Scale bar = 5 μm. Full panels shown of images provided in Figure 6D. (**A**-
1130 **D**) Data represent the mean ± S.E.M. * $p < 0.05$ by Student t test (**A**-**C**).

1131

1132

1133 **Figure S5. Dual mCherry+ proCpepSNAP+ reporter expression in primary mouse β-cells.**

1134 Mouse islets were co-treated with AdRIP-proCpepSNAP and either Ad-shRNA-SAFE (control)

1135 or Ad-shRNA-Idh1 and analyzed after 72 h. Mouse islets were pulse-labeled with SNAP-505

1136 for 20 min (green) and chased for 2 h. Cells were fixed, immunostained for GM130 (magenta),

1137 and counterstained with DAPI (blue). mCherry expression was used to identify shRNA-

1138 expressing cells in each condition for analysis (scale bar = 2 μm).

Figure 1

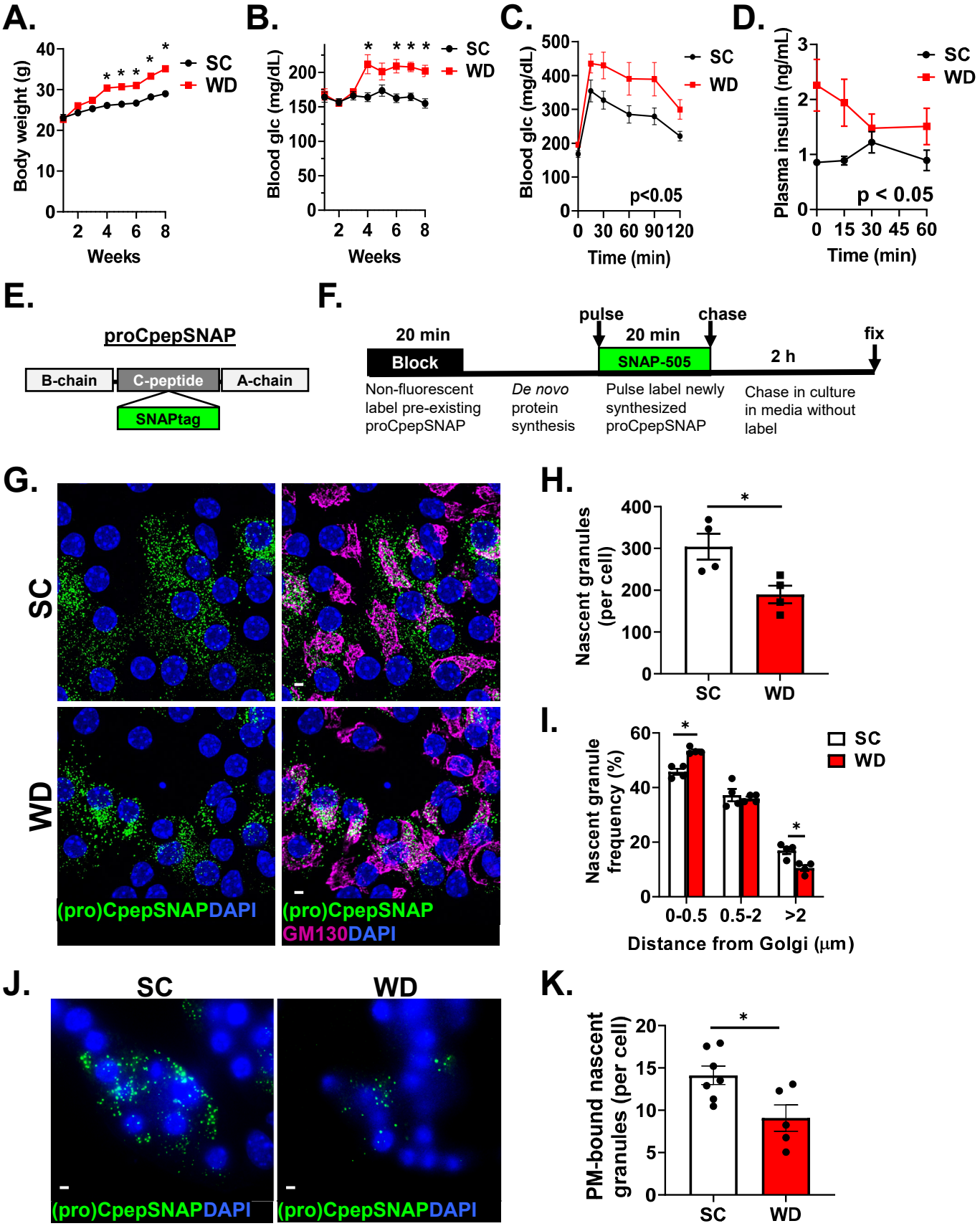
A.
Body weight (g)
Weeks
SC
WD
B.
Blood glc (mg/dL)
Weeks
SC
WD
C.
Blood glc (mg/dL)
Time (min)
SC
WD
p<0.05
D.
Plasma insulin (ng/mL)
Time (min)
SC
WD
p < 0.05
E.
proCpepSNAP
B-chain
C-peptide
A-chain
SNAPtag
F.
20 min
Block
pulse
20 min
SNAP-505
chase
2 h
fix
Non-fluorescent label pre-existing proCpepSNAP
De novo protein synthesis
Pulse label newly synthesized proCpepSNAP
Chase in culture in media without label
G.
SC
WD
(pro)CpepSNAPDAPI
(pro)CpepSNAP
GM130DAPI
H.
Nascent granules (per cell)
SC
WD
I.
Nascent granule frequency (%)
SC
WD
0-0.5
0.5-2
>2
Distance from Golgi (μm)
J.
SC
WD
(pro)CpepSNAPDAPI
(pro)CpepSNAPDAPI
K.
PM-bound nascent granules (per cell)
SC
WD

Figure 2

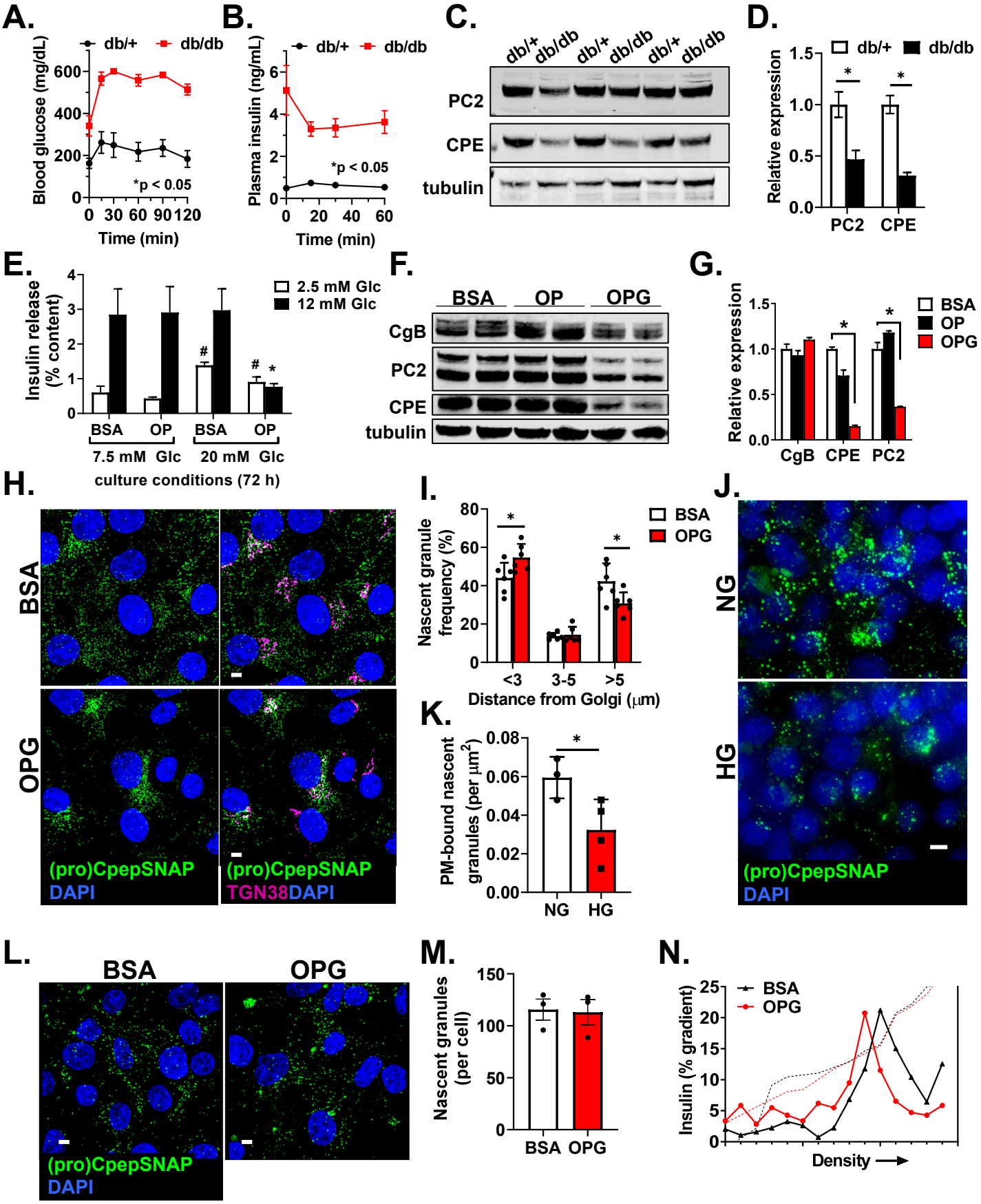
A.
db/+
db/db
Blood glucose (mg/dL)
600
400
200
0
*p < 0.05
0 30 60 90 120
Time (min)
B.
db/+
db/db
Plasma insulin (ng/mL)
6
4
2
0
*p < 0.05
0 20 40 60
Time (min)
C.
db/+ db/db db/+ db/db db/+ db/db
PC2
CPE
tubulin
D.
db/+
db/db
Relative expression
1.5
1.0
0.5
0.0
*
*
PC2 CPE
E.
Insulin release (% content)
4
3
2
1
0
2.5 mM Glc
12 mM Glc
#
#
*
BSA OP BSA OP
7.5 mM Glc
20 mM Glc
culture conditions (72 h)
F.
BSA OP OPG
CgB
PC2
CPE
tubulin
G.
Relative expression
1.5
1.0
0.5
0.0
BSA
OP
OPG
*
*
CgB CPE PC2
H.
BSA
OPG
(pro)CpepSNAP
DAPI
(pro)CpepSNAP
TGN38DAPI
I.
Nascent granule frequency (%)
80
60
40
20
0
BSA
OPG
*
*
<3 3-5 >5
Distance from Golgi (μm)
J.
NG
HG
(pro)CpepSNAP
DAPI
K.
PM-bound nascent granules (per μm²)
0.08
0.06
0.04
0.02
0.00
*
NG HG
L.
BSA
OPG
(pro)CpepSNAP
DAPI
M.
Nascent granules (per cell)
150
100
50
0
BSA OPG
N.
Insulin (% gradient)
25
20
15
10
5
0
BSA
OPG
Density

Figure 3

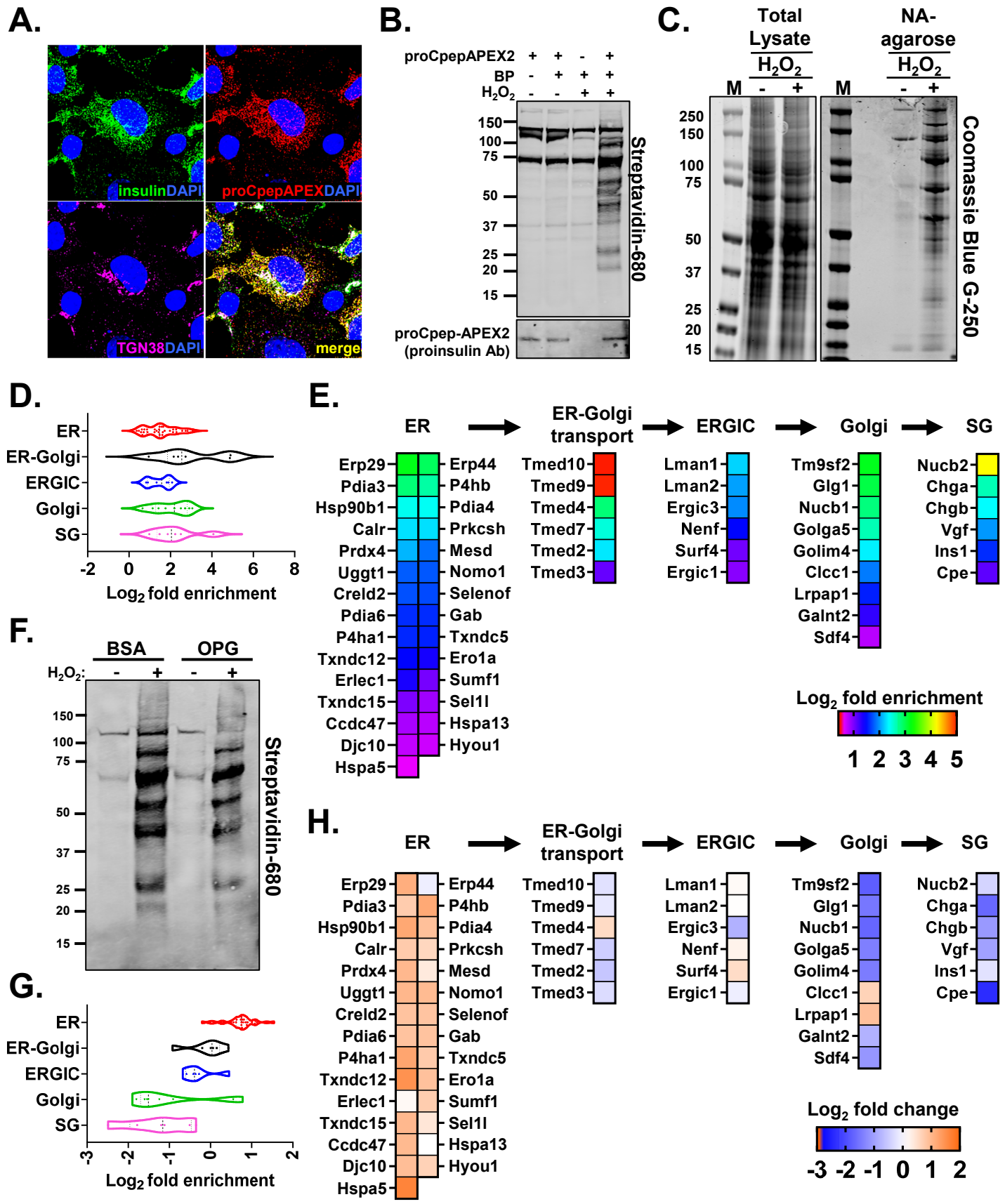
A.
insulinDAPI
proCpepAPEXDAPI
TGN38DAPI
merge
B.
proCpepAPEX2 + + - +
BP - + + +
H2O2 - - + +
150
100
75
50
37
25
20
15
Streptavidin-680
proCpep-APEX2
(proinsulin Ab)
C.
Total Lysate
NA-agarose
H2O2
M - +
250
150
100
75
50
37
25
20
15
Coomassie Blue G-250
D.
ER
ER-Golgi
ERGIC
Golgi
SG
-2 0 2 4 6 8
Log2 fold enrichment
E.
ER
ER-Golgi transport
ERGIC
Golgi
SG
Erp29
Pdia3
Hsp90b1
Calr
Prdx4
Uggt1
Creld2
Pdia6
P4ha1
Txndc12
Erlec1
Txndc15
Ccdc47
Djc10
Hspa5
Erp44
P4hb
Pdia4
Prkcsh
Mesd
Nomo1
Selenof
Gab
Txndc5
Ero1a
Sumf1
Sel1l
Hspa13
Hyou1
Tmed10
Tmed9
Tmed4
Tmed7
Tmed2
Tmed3
Lman1
Lman2
Ergic3
Nenf
Surf4
Ergic1
Tm9sf2
Glg1
Nucb1
Golga5
Golim4
Clcc1
Lrpap1
Galnt2
Sdf4
Nucb2
Chga
Chgb
Vgf
Ins1
Cpe
Log2 fold enrichment
1 2 3 4 5
F.
BSA
OPG
H2O2: - + - +
150
100
75
50
37
25
20
15
Streptavidin-680
G.
ER
ER-Golgi
ERGIC
Golgi
SG
-3 -2 -1 0 1 2
Log2 fold enrichment
H.
ER
ER-Golgi transport
ERGIC
Golgi
SG
Log2 fold change
-3 -2 -1 0 1 2

Figure 4

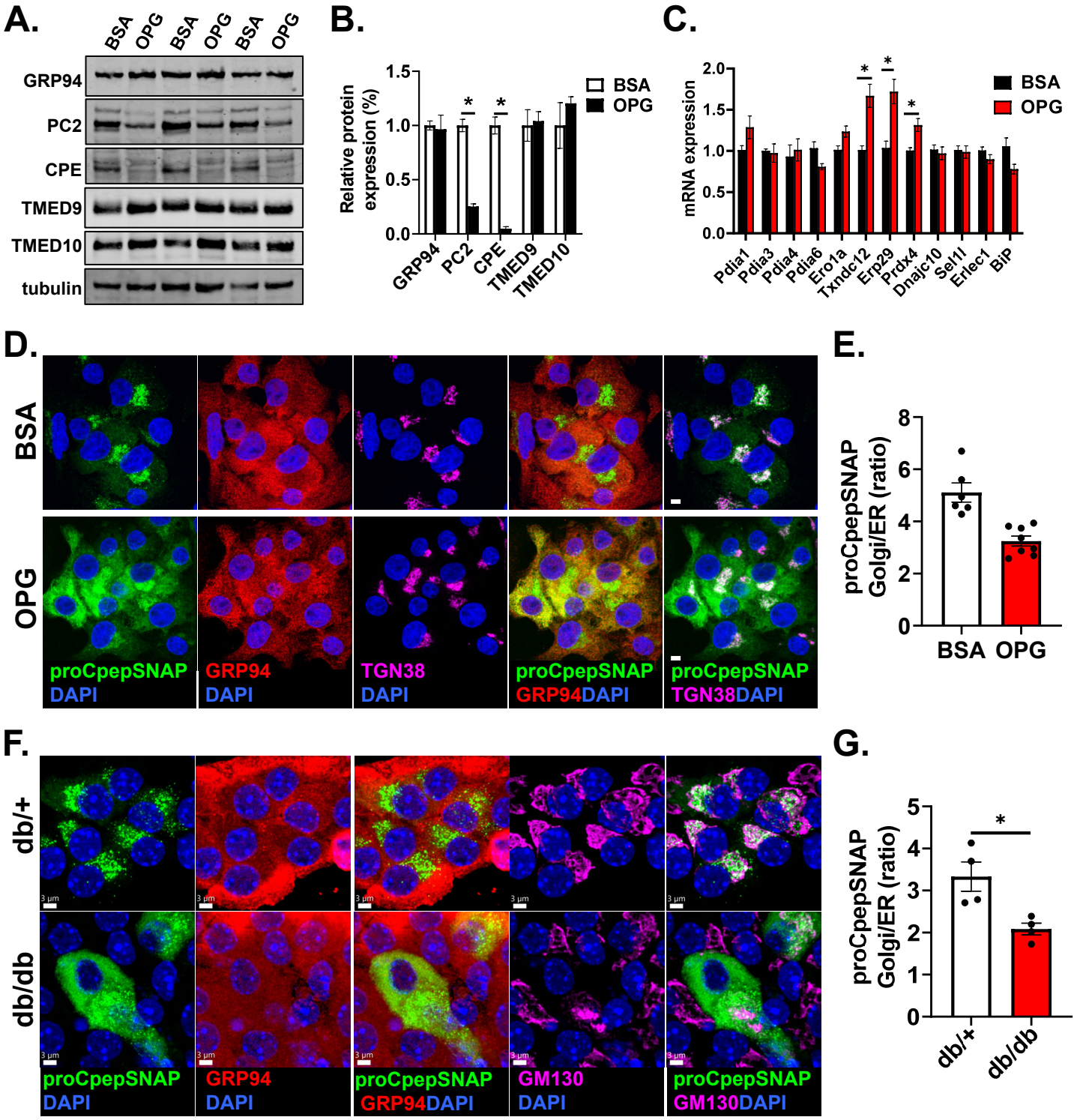
A.
BSA
OPG
BSA
OPG
BSA
OPG
GRP94
PC2
CPE
TMED9
TMED10
tubulin
B.
Relative protein expression (%)
1.5
1.0
0.5
0.0
BSA
OPG
GRP94
PC2
CPE
TMED9
TMED10
C.
mRNA expression
2.0
1.5
1.0
0.5
0.0
BSA
OPG
Pdia1
Pdia3
Pdia4
Pdia6
Ero1a
Txndc12
Erp29
Prdx4
Dnajc10
Sel1l
Erlec1
BiP
D.
BSA
OPG
proCpepSNAP
DAPI
GRP94
DAPI
TGN38
DAPI
proCpepSNAP
GRP94DAPI
proCpepSNAP
TGN38DAPI
E.
proCpepSNAP Golgi/ER (ratio)
8
6
4
2
0
BSA
OPG
F.
db/+
db/db
proCpepSNAP
DAPI
GRP94
DAPI
proCpepSNAP
GRP94DAPI
GM130
DAPI
proCpepSNAP
GM130DAPI
G.
proCpepSNAP Golgi/ER (ratio)
5
4
3
2
1
0
db/+
db/db

Figure 5

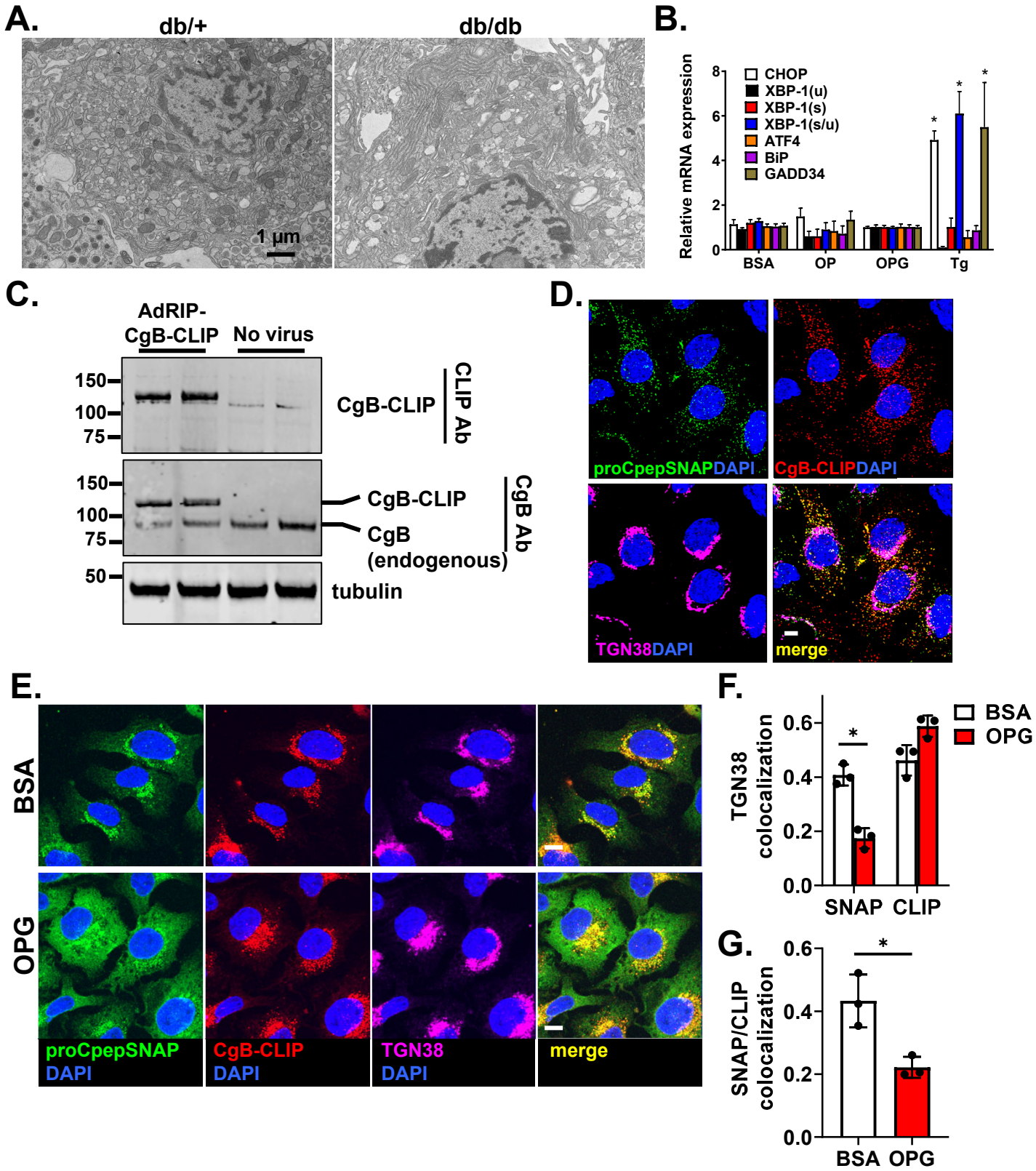
A.
db/+
db/db
1 µm
B.
Relative mRNA expression
CHOP
XBP-1(u)
XBP-1(s)
XBP-1(s/u)
ATF4
BiP
GADD34
BSA
OP
OPG
Tg
C.
AdRIP-CgB-CLIP
No virus
150
100
75
50
CgB-CLIP
CLIP Ab
CgB-CLIP
CgB (endogenous)
CgB Ab
tubulin
D.
proCpepSNAPDAPI
CgB-CLIPDAPI
TGN38DAPI
merge
E.
BSA
OPG
proCpepSNAP DAPI
CgB-CLIP DAPI
TGN38 DAPI
merge
F.
TGN38 colocalization
BSA
OPG
SNAP
CLIP
G.
SNAP/CLIP colocalization
BSA
OPG

Figure 6

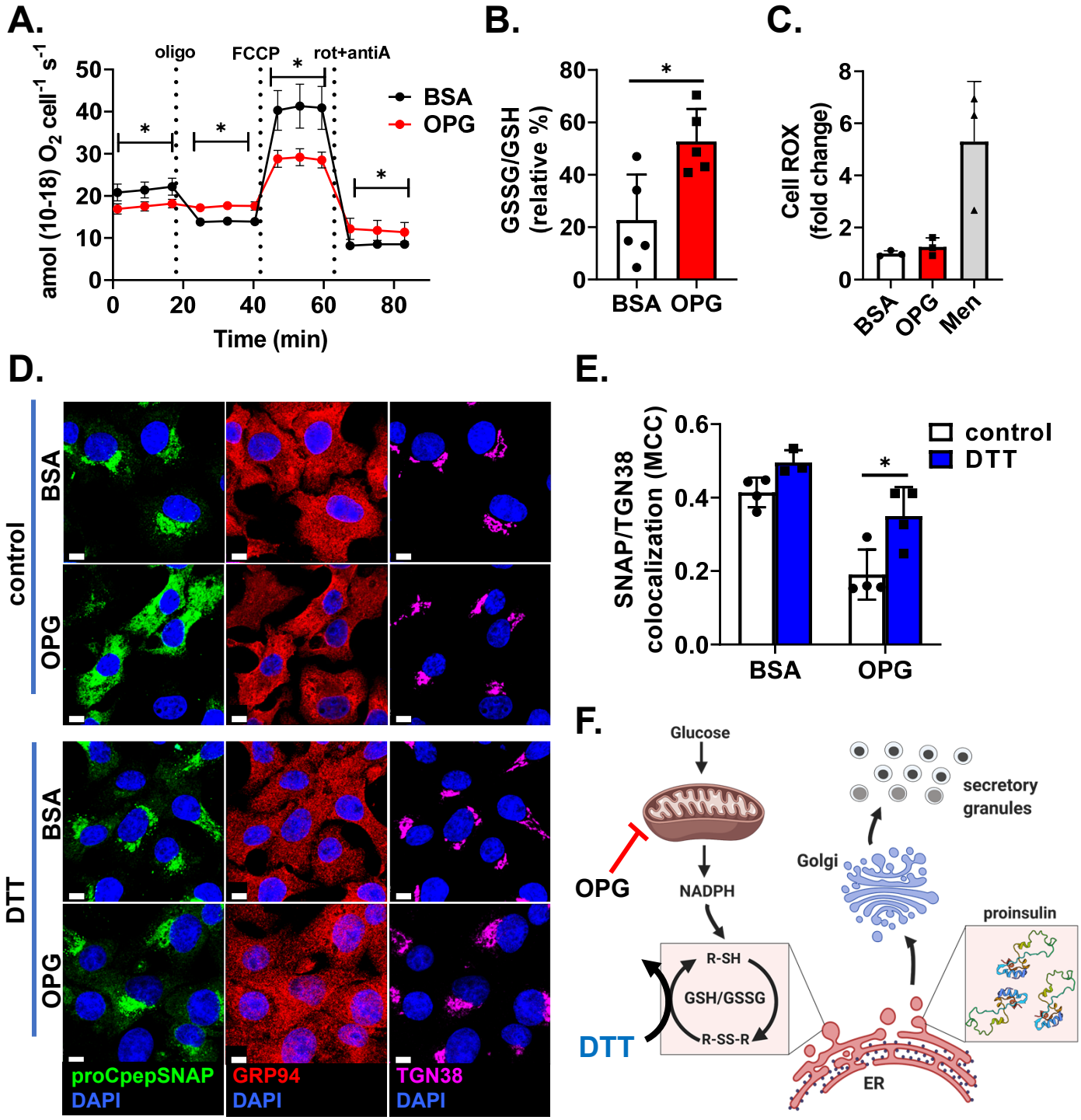
A.
oligo
FCCP
rot+antiA
BSA
OPG
amol (10-18) O2 cell-1 s-1
Time (min)
B.
GSSG/GSH (relative %)
BSA
OPG
C.
Cell ROX (fold change)
BSA
OPG
Men
D.
control
DTT
BSA
OPG
proCpepSNAP
DAPI
GRP94
DAPI
TGN38
DAPI
E.
SNAP/TGN38 colocalization (MCC)
control
DTT
BSA
OPG
F.
Glucose
OPG
NADPH
R-SH
GSH/GSSG
R-SS-R
DTT
Golgi
secretory granules
proinsulin
ER

Figure 7

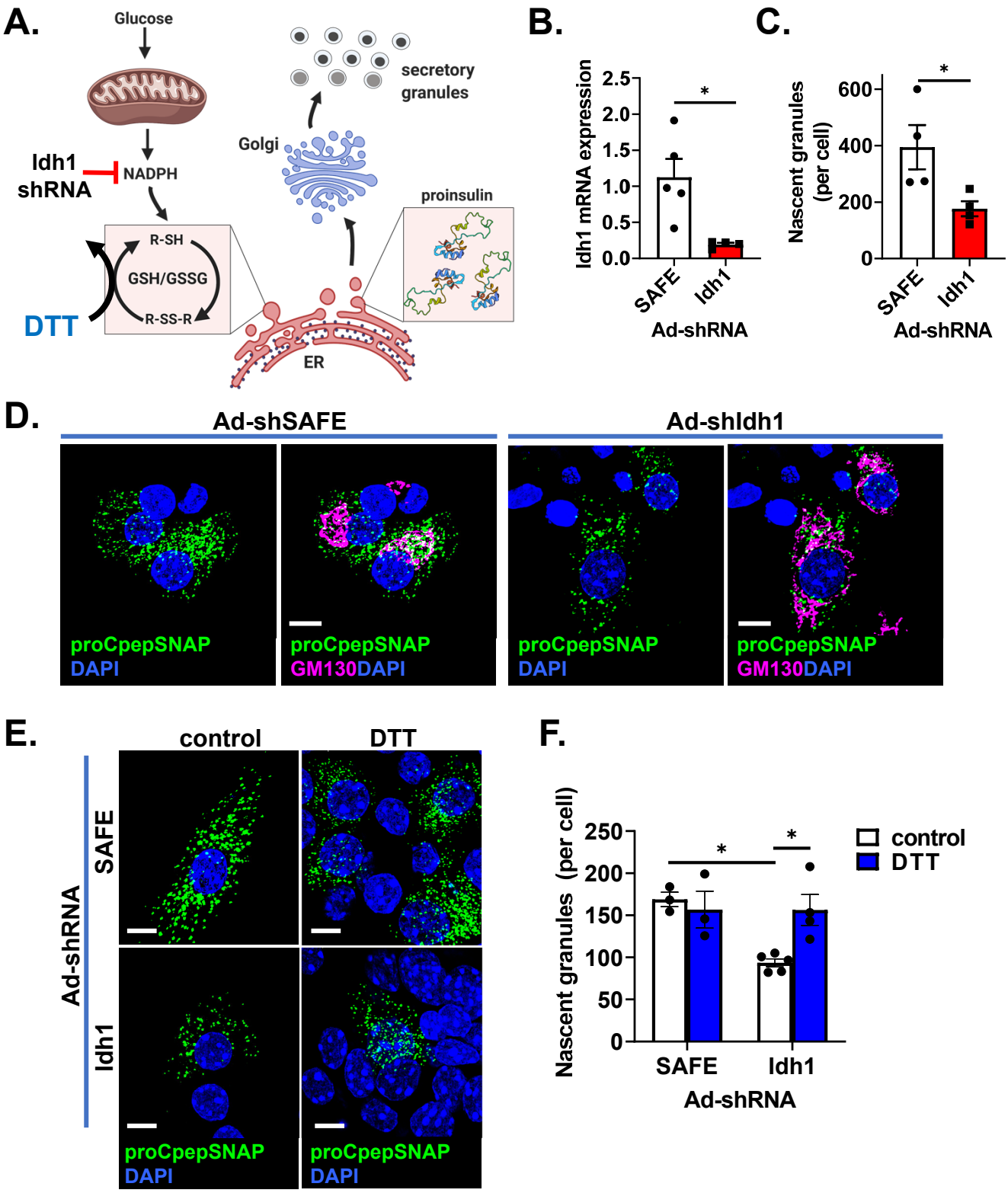
A.
Glucose
Idh1
shRNA
NADPH
R-SH
GSH/GSSG
R-SS-R
DTT
Golgi
secretory
granules
proinsulin
ER
B.
Idh1 mRNA expression
2.5
2.0
1.5
1.0
0.5
0.0
*
SAFE
Idh1
Ad-shRNA
C.
Nascent granules
(per cell)
600
400
200
0
*
SAFE
Idh1
Ad-shRNA
D.
Ad-shSAFE
Ad-shIdh1
proCpepSNAP
DAPI
proCpepSNAP
GM130DAPI
proCpepSNAP
DAPI
proCpepSNAP
GM130DAPI
E.
control
DTT
Ad-shRNA
SAFE
Idh1
proCpepSNAP
DAPI
proCpepSNAP
DAPI
F.
Nascent granules (per cell)
250
200
150
100
50
0
*
*
control
DTT
SAFE
Idh1
Ad-shRNA

Figure 8

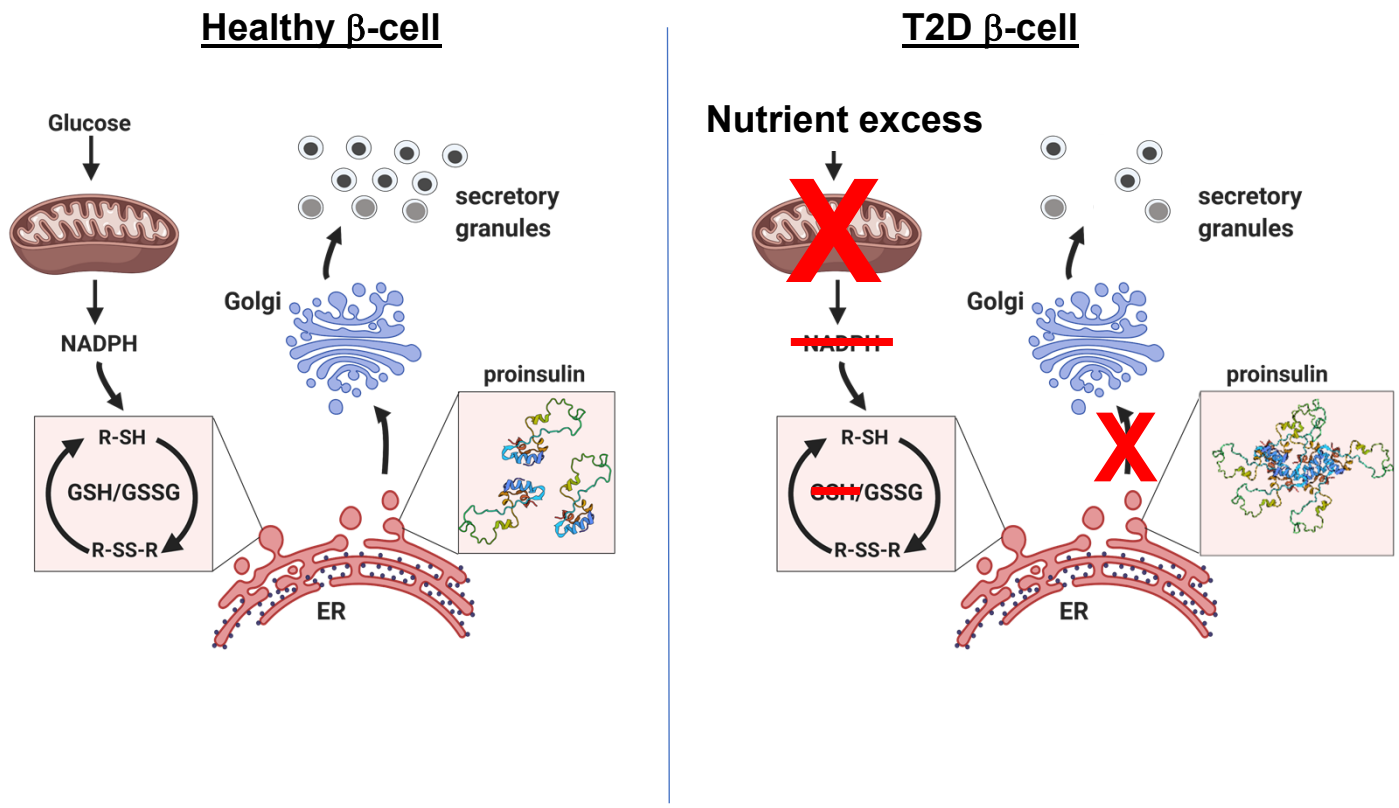
Healthy β-cell
Glucose
NADPH
R-SH
GSH/GSSG
R-SS-R
Golgi
secretory granules
proinsulin
ER
T2D β-cell
Nutrient excess
NADPH
R-SH
GSH/GSSG
R-SS-R
Golgi
secretory granules
proinsulin
ER

Figure S1

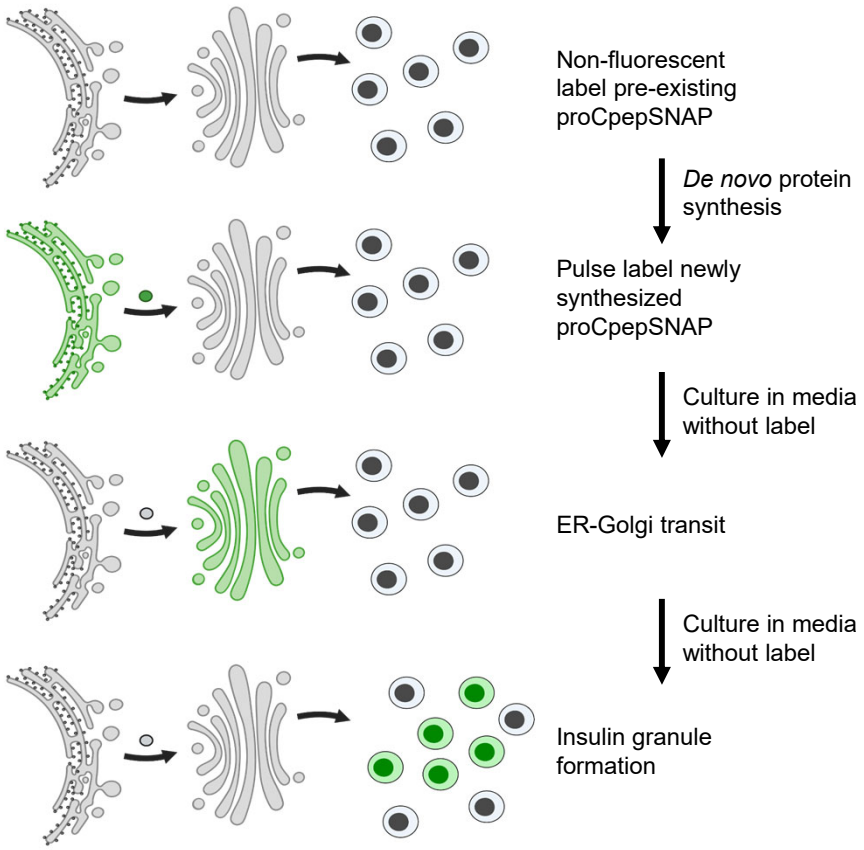
Non-fluorescent
label pre-existing
proCpepSNAP
De novo protein
synthesis
Pulse label newly
synthesized
proCpepSNAP
Culture in media
without label
ER-Golgi transit
Culture in media
without label
Insulin granule
formation

Figure S2

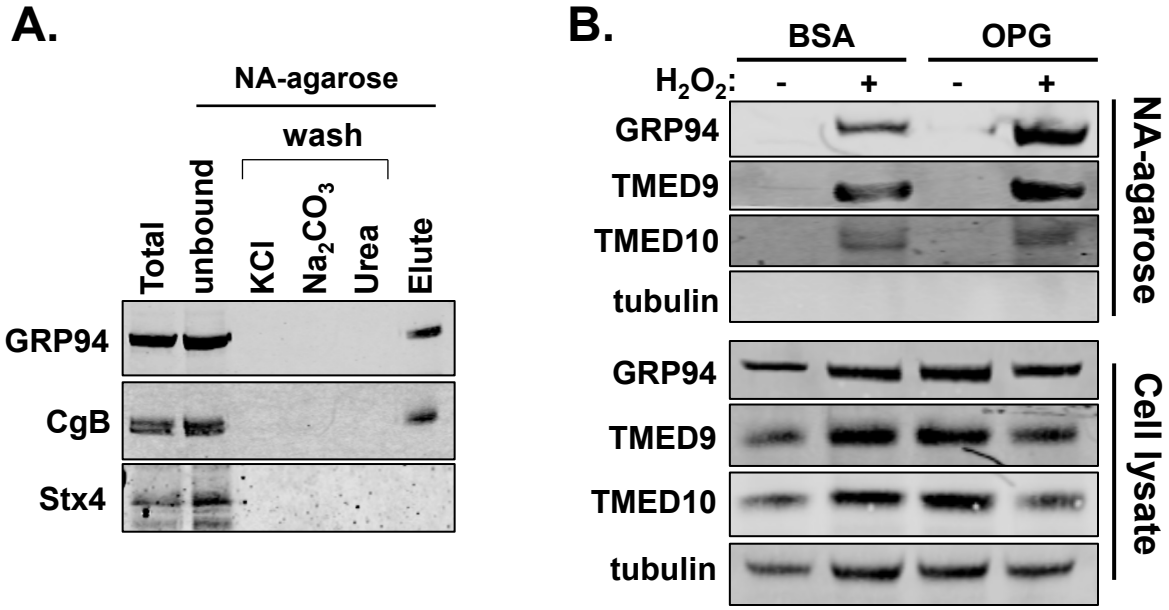
A.
NA-agarose
wash
Total
unbound
KCl
Na_2CO_3
Urea
Elute
GRP94
CgB
Stx4
B.
BSA
OPG
H_2O_2:
-
+
-
+
GRP94
TMED9
TMED10
tubulin
NA-agarose
GRP94
TMED9
TMED10
tubulin
Cell lysate

Figure S3

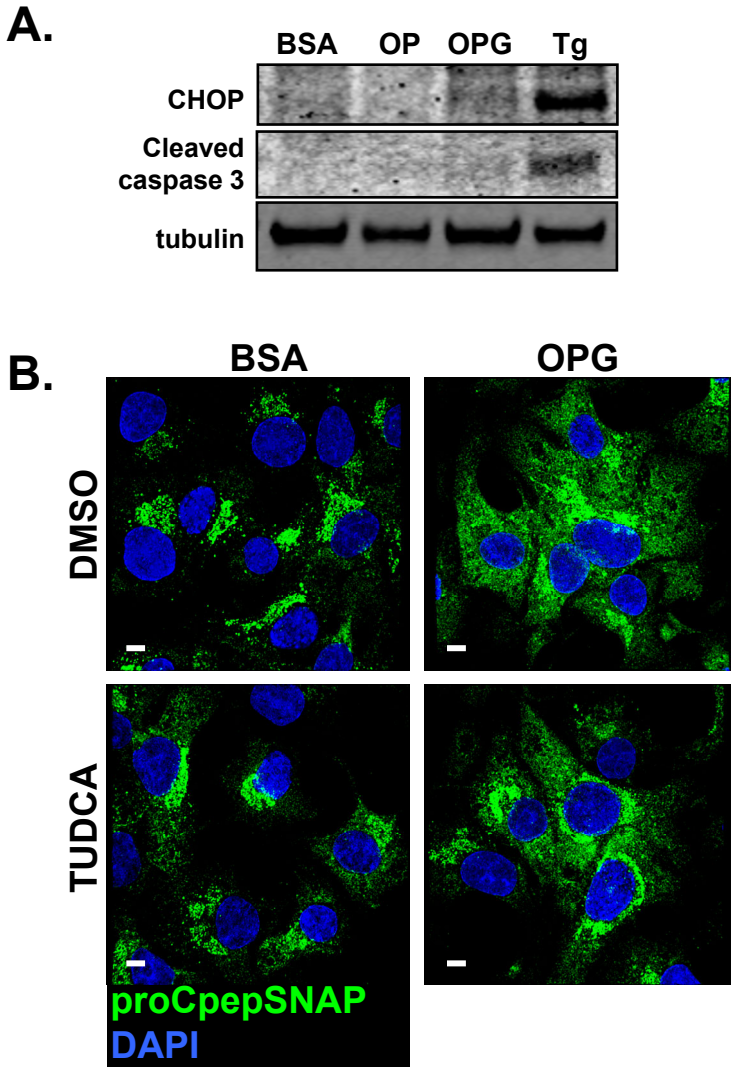
A.
BSA
OP
OPG
Tg
CHOP
Cleaved caspase 3
tubulin
B.
BSA
OPG
DMSO
TUDCA
proCpepSNAP
DAPI

Figure S4

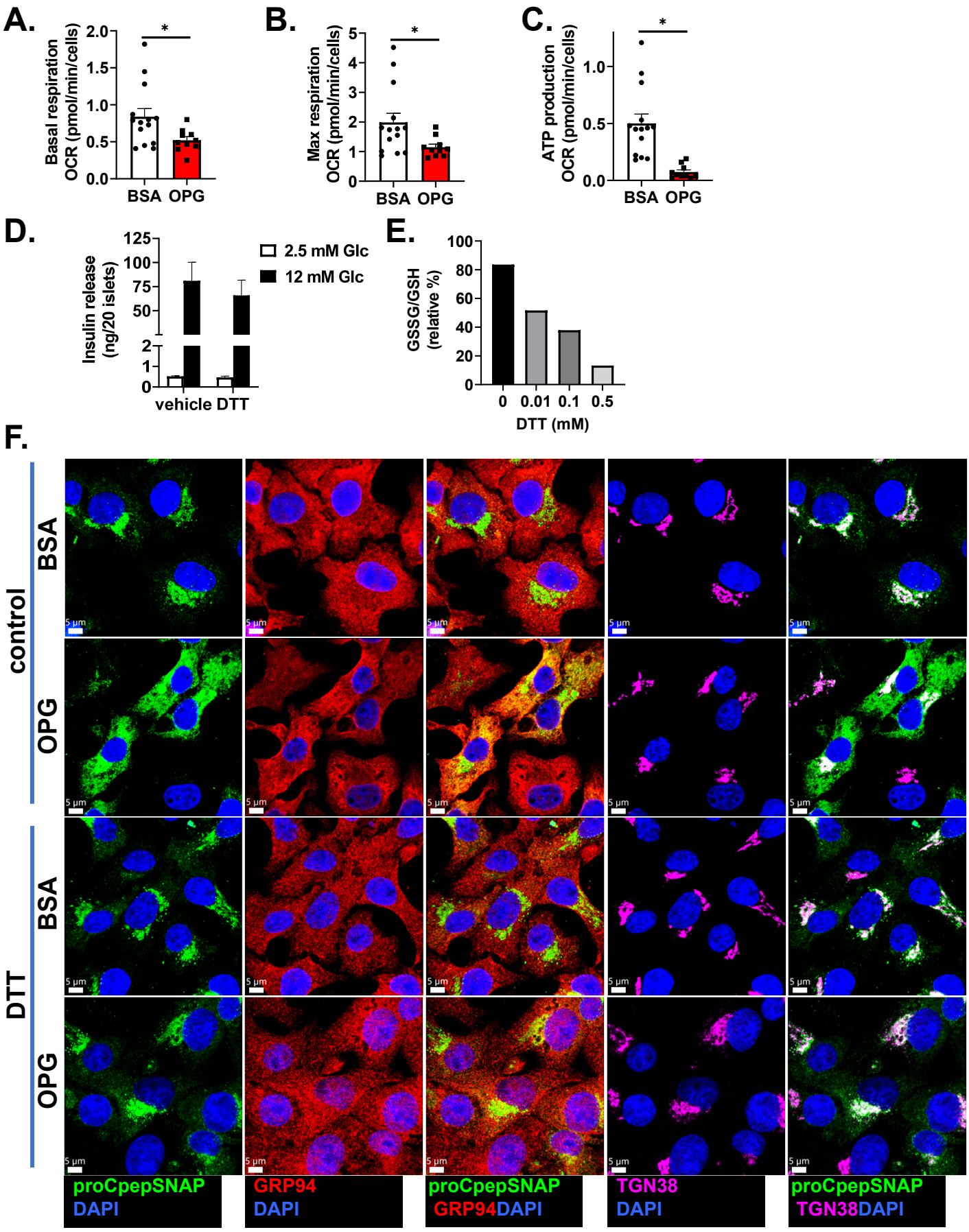
A.
Basal respiration OCR (pmol/min/cells)
2.0
1.5
1.0
0.5
0.0
*
BSA
OPG
B.
Max respiration OCR (pmol/min/cells)
5
4
3
2
1
0
*
BSA
OPG
C.
ATP production OCR (pmol/min/cells)
1.0
0.5
0.0
*
BSA
OPG
D.
Insulin release (ng/20 islets)
125
100
75
50
2
1
0
2.5 mM Glc
12 mM Glc
vehicle
DTT
E.
GSSG/GSH (relative %)
100
80
60
40
20
0
0
0.01
0.1
0.5
DTT (mM)
F.
control
BSA
OPG
DTT
BSA
OPG
5 µm
proCpepSNAP
DAPI
GRP94
DAPI
proCpepSNAP
GRP94DAPI
TGN38
DAPI
proCpepSNAP
TGN38DAPI

Figure S5

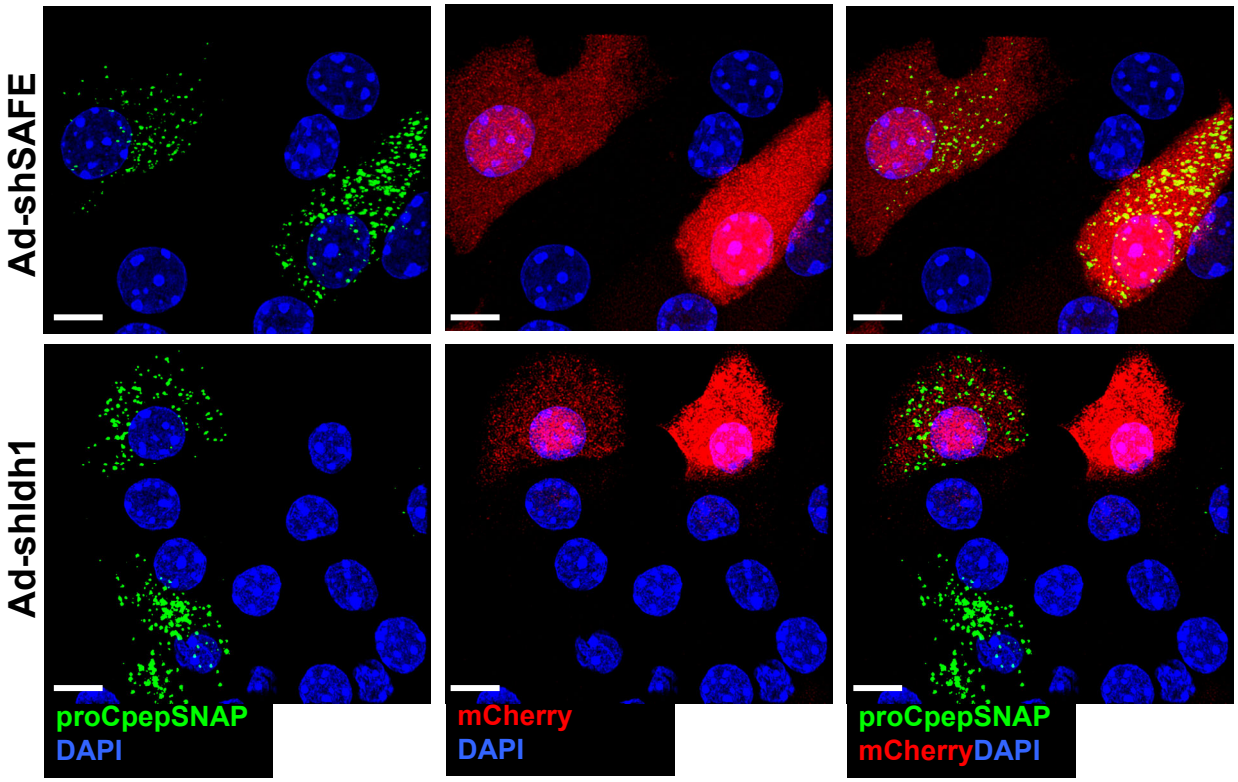
Ad-shSAFE
Ad-shldh1
proCpepSNAP
DAPI
mCherry
DAPI
proCpepSNAP
mCherryDAPI